Check for updates

ChemPhotoChem

Chemistry Europe
European Chemical Societies Publishing
ChemPhotoChem

RESEARCH ARTICLE OPEN ACCESS

A Water-Soluble Fluorescent 2,5-bis(arylethynyl) rhodacyclopentadiene for Live-Cell Imaging and Sensing of DNA, RNA, and Protein (BSA)

Shishir Ghosh[1] | Florian Kerner[1] | Tim Görlich[1] | Alexandra Friedrich[1] | Sabine Lorenzen[1] | Jörn Nitsch[1] | Evripidis Michail[2] | Christoph Lambert[2] | Anissa Amar[3,4] | Abdou Boucekkine[5] | Jean-François Halet[5] | Marta Jurković[6] | Ksenija Božinović[7] | Ivo Piantanida[6] | Todd B. Marder[1]

[1]Institut für Anorganische Chemie, Julius-Maximilians-Universität Würzburg, Würzburg, Germany | [2]Institut für Organische Chemie, Julius-Maximilians-Universität Würzburg, Würzburg, Germany | [3]Laboratoire de Thermodynamique et de Modélisation Moléculaire, Faculté de Chimie, USTHB, Bab-Ezzouar, Algeria | [4]Laboratoire de Physique et Chimie Quantiques, Faculté des Sciences, UMMTO, Tizi-Ouzou, Algeria | [5]Univ Rennes, CNRS, Ecole Nationale Supérieure de Chimie de Rennes (ENSCR), Institut des Sciences Chimiques de Rennes (ISCR), UMR 6226, Rennes, France | [6]Laboratory for Study of Interactions of Biomacromolecules, Division of Organic Chemistry & Biochemistry, Ruđer Bošković Institute, Zagreb, Croatia | [7]Division of Molecular Biology, Ruđer Bošković Institute, Zagreb, Croatia

Correspondence: Ivo Piantanida (Ivo.Piantanida@irb.hr) | Todd B. Marder (todd.marder@uni-wuerzburg.de)

Received: 9 March 2026 | **Revised:** 6 July 2026 | **Accepted:** 14 July 2026

Keywords: biomolecule sensing | cell imaging | DFT and TD-DFT calculations | fluorescence | metallacycle

ABSTRACT

A water-soluble and water-stable 2,5-bis(arylethynyl)rhodacyclopentadiene (**4a**) containing terminal 4-Me_3N–C_6H_4 groups has been synthesized for bioimaging and sensing of biomolecules, and its linear and nonlinear optical properties investigated. Complex **4a** exhibits fluorescence from the S_1 excited state in both organic and aqueous solutions, with no observable phosphorescence from T_1 at RT. However, competitive intersystem crossing (ISC) to T_1 leads to potent $^1O_2$ sensitization. DFT calculations show that the HOMO and LUMO are essentially ligand-localized with very modest contributions from Rh, leading to slow $S_1 \rightarrow T_1$ ISC and competitive fluorescence and triplet state formation, typical of such 2,5-bis(arylethynyl)rhodacyclopentadienes. Complex **4a** shows a two-photon absorption cross-section of 290 GM at 680 nm. It binds strongly to DNA, RNA, and protein (BSA) with similar affinities, but gives opposite fluorimetric response, the emission being strongly enhanced for BSA but efficiently quenched by DNA/RNA. Compound **4a** efficiently enters living human cells and accumulates preferentially in mitochondrial membranes, being nontoxic even at high (10 μM) concentrations. Although **4a** is a potent $^1O_2$ sensitizer in a cuvette, exposure of the complex to intense visible light inside human cell results in fast bleaching of **4a** with no effect on cell viability, suggesting local consumption of $^1O_2$ by the complex.

1 | Introduction

Photoluminescent transition metal complexes have brought new perspectives to bioimaging as they offer potential advantages over conventional organic molecules/dyes typically used for this purpose. For example, the synthetic versatility of transition metal complexes allows for their preparation through well-defined strategies, often involving stepwise introduction of different ligands, as well as their often-straightforward purification via chromatography or crystallization, whereas modification of many fluorescent organic systems can be demanding. The photophysical properties of metal complexes such as tunability of luminescence

Dedicated to the memory of Prof. Dr. Davit Zargarian.

This is an open access article under the terms of the Creative Commons Attribution License, which permits use, distribution and reproduction in any medium, provided the original work is properly cited.

© 2026 The Author(s). *ChemPhotoChem* published by Wiley-VCH GmbH.

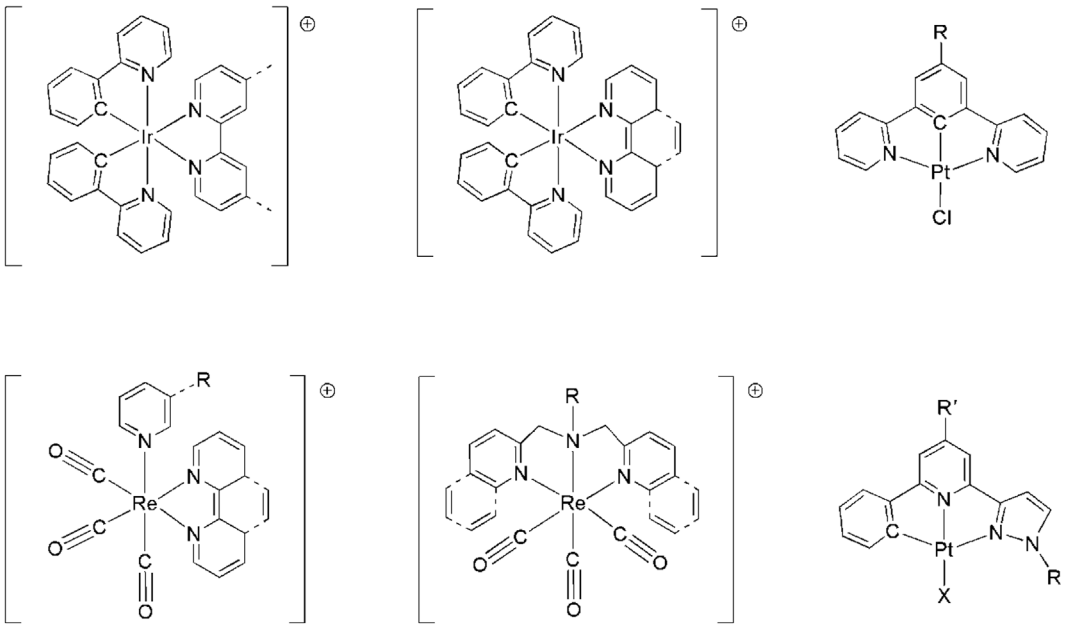

SCHEME 1 | Structures of the core units of some typical organometallic iridium, platinum, and rhenium complexes used in bioimaging.

can be controlled with greater ease than organic systems, and they are also typically more resistant to photobleaching compared to their organic counterparts. In addition, the long emission lifetimes of phosphorescent metal complexes make them suitable candidates for use in time-gated detection techniques such as time-resolved luminescence microscopy (TRLM) and fluorescence lifetime imaging microscopy (FLIM). Hence, the design and development of metal-based probes for bioimaging is a subject of considerable interest in contemporary science [1–24].

One potential disadvantage of using long-lived emitters in bioimaging is the potential for quenching of the excited state by entities such as dissolved molecular oxygen as the long emission lifetime allows more time for excited-state quenching processes to occur. This often leads to the formation of singlet oxygen ($^1O_2$) [25], which is very reactive toward organic molecules and biological entities. This can lead to phototoxicity, a desirable feature in photodynamic therapy (PDT) [26], for example, but obviously not for phosphorescent imaging purposes. This, however, also suggests the possibility of using fluorescent emitters which undergo competitive intersystem crossing (ISC) to their triplet states capable of sensitizing $^1O_2$ in combined imaging and therapy, i.e., as a theranostic agent [27].

While a variety of metal complexes have found applications in bioimaging [1–24], very few organometallic systems have been used for this purpose thus far [15–18]. The most widely studied organometallic systems used for bioimaging are iridium and platinum cyclometalates containing, for example, ubiquitous 2-phenylpyridine as a cyclometalated ligand [28–34] and octahedral rhenium *fac*-tricarbonyl complexes incorporating polypyridine and quinoline moieties [35–38] (Scheme 1). The platinum cyclometalates are capable of two-photon excitation which allows deep tissue penetration with efficient excitation using a near-IR laser source at wavelengths where biological tissue is relatively transparent (the biological window), thus having the potential to be developed as very powerful imaging probes [30, 32–34]. A few organometallic complexes of gold, typically Au(I) species as they are known to exhibit luminescence through a variety of mechanisms [39], have also been used for bioimaging [40, 41]. Related studies on their therapeutic abilities showed that these Au(I) luminophores could potentially be developed for use in combined imaging and therapy [41, 42].

Our long-standing interest in MC_4 metallacyclopentadienes led us to the development of a regioselective, high-yielding synthetic route for the preparation of octahedral 2,5-bis(arylethynyl)rhodacyclopenta-2,4-dienes (**A**) and related rhodium biphenyl complexes (**B**) over the past two decades (Scheme 2) [43–48]. The rhodacyclopentadienes (**A**) exhibit fluorescence with quantum yields up to $\Phi_{PL} = 0.69$ despite the presence of a second-row

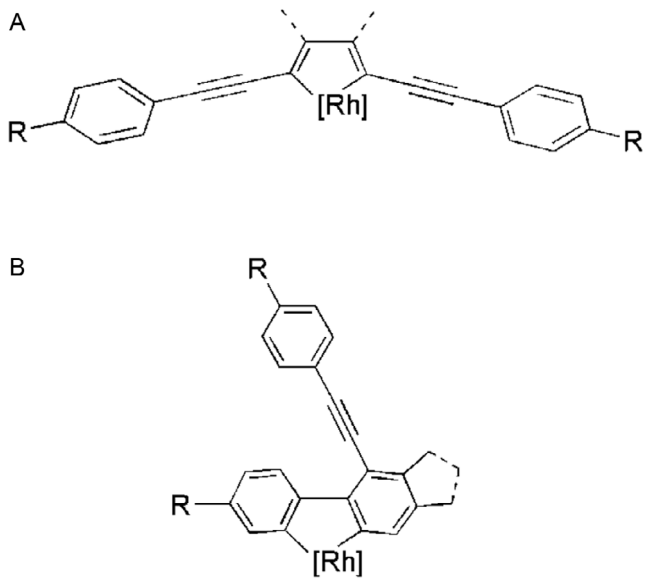

SCHEME 2 | Structures of the core units of luminescent (A) 2,5-bis(arylethynyl)rhodacyclopenta-2,4-dienes and (B) rhodium biphenyl complexes.

23670932, 2026, 8, Downloaded from https://chemistry-europe.onlinelibrary.wiley.com/doi/10.1002/cptc.70228 by Cochrane Croatia, Wiley Online Library on [24/11/2026]. See the Terms and Conditions (https://onlinelibrary.wiley.com/terms-and-conditions) on Wiley Online Library for rules of use; OA articles are governed by the applicable Creative Commons License

transition metal but, interestingly, no observable phosphorescence even at 77 K in a glass matrix [44–46]. These rhodacyclopentadienes (**A**) are also found to act as potent sensitizers of singlet oxygen ($^1O_2$) [44–46]. In contrast, the biphenyl complexes (**B**) show purely phosphorescence as expected of complexes bearing a second-row transition metal [47]. A picosecond time-resolved IR spectroscopic investigation confirmed that the ISC in rhodacyclopentadienes (**A**) is unusually slow [44], occurring in nanosecond timescale instead of in the order of femto- or picoseconds as expected for octahedral organometallic complexes [39], thus being competitive with fluorescence, whereas the fast ISC process in biphenyl complexes (**B**) makes them phosphorescent [47].

Theoretical investigations revealed that the frontier molecular orbitals (MOs) in **A** are nearly pure ligand-based π and π* MOs that are also energetically isolated from the other filled and vacant MOs which inhibits low-energy MLCT transitions and hampers the ISC process [45, 47]. In contrast, the frontier MOs in **B** are mixtures of ligand π and metal d orbitals with the HOMO being energetically close to other filled MOs having significant contribution from the metal [47]. Hence, a series of triplet excited states with some MLCT contribution exists in **B** which can efficiently connect the S_1 state with the emitting T_1 state [47]. The biphenyl complexes (**B**) also exhibit exceptionally long emission lifetimes on the timescale of tens to hundreds of microseconds at room temperature [47], and we have successfully used one of these complexes in a bimetallic photocatalytic system as a triplet sensitizer that also consists of the nickel catalyst [Ni(IMes)$_2$] (IMes = 1,3-dimesitylimidazol-2-ylidene) for the borylation of C—F bonds in aryl fluorides by taking advantage of this long-lived triplet excited state [49].

The fluorescent rhodacyclopentadienes (**A**) with the capability of singlet oxygen sensitization are, in principle, ideal candidates for combined imaging and therapy application. To probe this area of immense interest, we have now prepared a water-soluble derivative, namely, [Rh(κ^2-*O*,*O*-acac)(PMe$_3$)$_2$\{κ^2-CH$_2$(CH$_2$C═CC≡CC$_6$H$_4$NMe$_3$)$_2$\}][I]$_2$ (**4a**) (Scheme 3), and investigated its utility in bioimaging and/or PDT. We have also prepared an isotopologue of **4a**, i.e., **4b**, by replacing the PMe$_3$ ligands with P(CD$_3$)$_3$ and studied its photophysical properties in order to investigate whether the C—H vibrations of the PMe$_3$ ligands are involved in the non-radiative decay process of these rhodacyclopentadienes (**A**). Details of these investigations will be discussed herein.

In line with the aforementioned biological applications of some analogs (Scheme 1 and related references), we have also examined interactions of the novel compound with various DNA and RNA targets to assess their binding affinity and fluorimetric response in a biorelevant context. Additionally, we investigated interactions with serum albumin (BSA), the most abundant protein in plasma and a well-known transporter of diverse biorelevant small molecules, including numerous drugs.

2 | Results and Discussion

2.1 | Synthesis and Characterization

The synthetic protocol for the preparation of targeted rhodacyclopentadiene **4** is illustrated in Scheme 3. As direct reaction of our linked bisdiynes with [Rh(κ^2-*O*,*O*-acac)\{(P(Me$_3$)$_2$\}] leads predominantly to the biphenyl complexes of type **B**, whereas analogous reaction with a triarylphosphine Rh precursor leads to the rhodacyclopentadienes of type **A** [47], the square-planar rhodium complex [Rh(κ^2-*O*,*O*-acac)\{(P(C$_6$H$_4$CH$_3$-*p*)$_3$\}$_2$] [48] was first reacted with 1,11-bis(*p*-*N*,*N*-dimethylaminophenyl)undeca-1,3,8,10-tetrayne (**1**) [47] at room temperature which afforded the octahedral rhodacyclopentadiene **2** via rhodium-mediated reductive coupling of alkynes. Then, **2** was treated with *ca*. 2 molar equivalents of PR$_3$ (R = Me, CD$_3$) at 40 °C to exchange the phosphine ligands, which led to the formation of **3**. Finally, methylation of the dimethylamino (NMe$_2$) functionalities of **3** at room temperature using MeI as the methylating agent gave

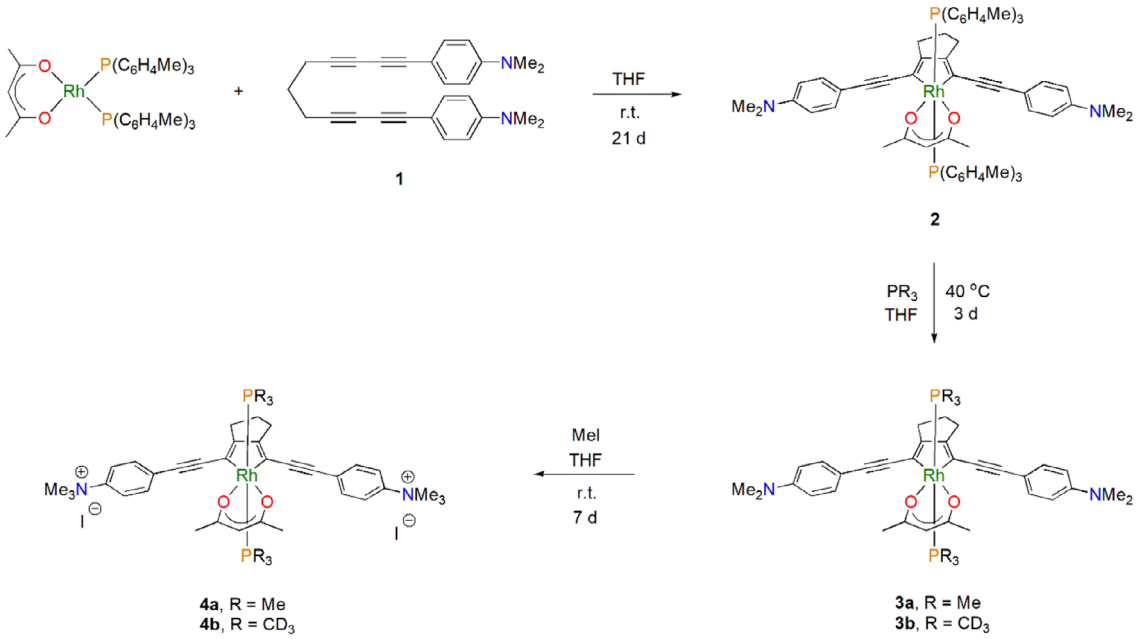

SCHEME 3 | Synthesis of 2,5-bis(arylethynyl)rhodacyclopentadienes **2**-**4**.

23670932, 2026, 8, Downloaded from https://chemistry-europe.onlinelibrary.wiley.com/doi/10.1002/cptc.70228 by Cochrane Croatia, Wiley Online Library on [24/11/2026]. See the Terms and Conditions (https://onlinelibrary.wiley.com/terms-and-conditions) on Wiley Online Library for rules of use; OA articles are governed by the applicable Creative Commons License

the desired rhodacyclopentadiene **4**. Complex **4** is highly soluble in methanol, while it also shows appreciable solubility in ethanol and water which were chosen for the measurement of its photophysical properties. It is air stable in the solid state but decomposes very slowly in organic solutions or in water when exposed to air (Figures S1–S4 in the Supporting Information).

The metalacyclic complexes **2**-**4** have been unambiguously characterized by a combination of elemental analysis, NMR, and high-resolution mass spectroscopic data, and their molecular structures have been confirmed by single crystal X-ray diffraction analyses. NMR spectroscopic data of **2**-**4** revealed that they adopt structures with C_{2v} symmetry in solution. Thus, each of these complexes shows only a singlet for the six methyl protons of the acac ligand in the ^{1}H NMR spectrum, while the ^{31}P{^{1}H} NMR spectra exhibit one doublet with $J_{Rh\text{-}P}$ values ranging between 109 and 117 Hz, which are typical of other related rhodacyclopentadienes bearing PMe_3 or $P(C_6H_4Me)_3$ ligands [43–48].

The solid-state molecular structures of **2**-**4** are depicted in Figure 1 and in the Supporting Information (Figures S5–S9), and selected bond lengths and angles are listed in Table 1. As the X-ray diffraction measurement is unable to differentiate the two isotopes of hydrogen [^{1}H and ^{2}D], we obtained identical results within experimental error for the pair of isotopologues **3a** and **3b** as well as for **4a** and **4b** from the diffraction studies. In all

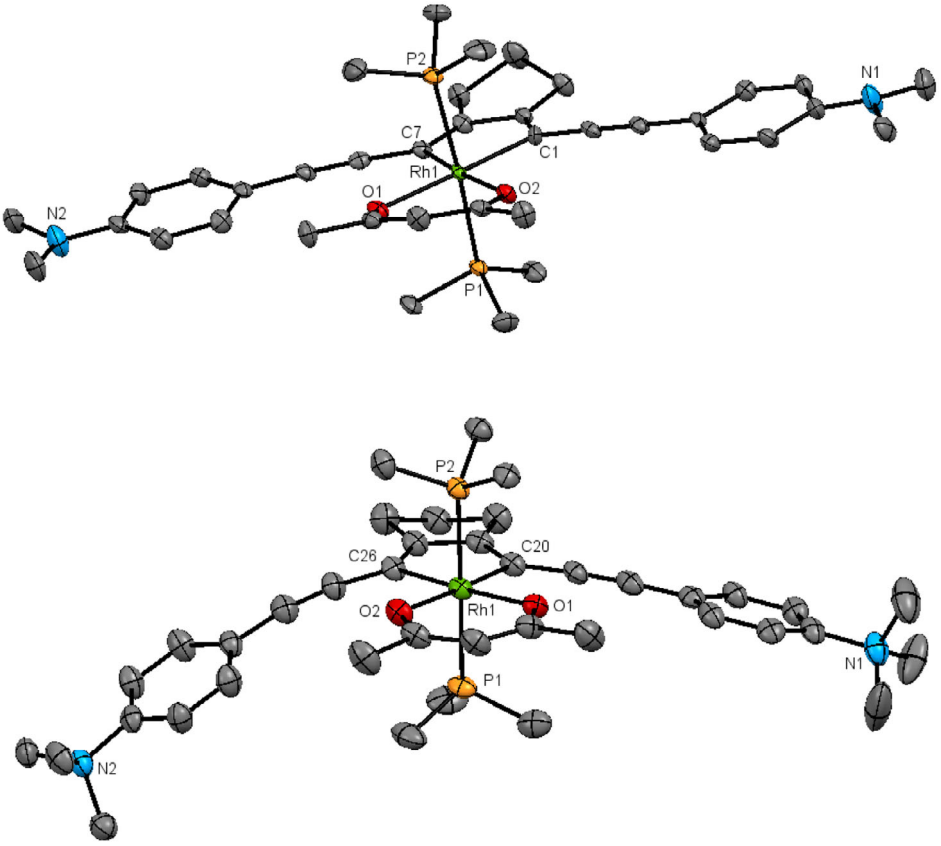

FIGURE 1 | Molecular structures of **3a** (top) and **4a** (bottom) at 100 K showing 50% probability atomic displacement ellipsoids. Hydrogen atoms and iodide ions (for **4a**) are omitted for clarity.

TABLE 1 | Selected bond lengths [Å] and bond angles [°] of compounds **2**, **3a**, **3b**, **4a**, and **4b**.

Compound	2	3a	3b	4a	4b
Rh–P	2.3508(10)	2.2950(14)	2.2958(6)	2.2957(13)	2.2948(8)
	2.3652(10)	2.3113(14)	2.3120(6)	2.3111(12)	2.3107(8)
Rh–C	2.039(2)	2.033(4)	2.0292(15)	2.029(5)	2.029(3)
	2.0470(17)	2.055(4)	2.0404(15)	2.037(5)	2.040(3)
Rh–O	2.1315(13)	2.135(3)	2.1356(11)	2.133(4)	2.132(2)
	2.1392(16)	2.141(3)	2.1487(11)	2.139(4)	2.137(2)
P–Rh–P	171.924(16)	175.31(4)	175.328(15)	178.87(5)	178.78(3)
C–Rh–C	81.02(7)	81.09(16)	81.04(6)	81.0(2)	80.79(13)
O–Rh–O	87.47(6)	88.61(10)	88.91(4)	89.47(15)	89.34(9)

23670932, 2026, 8, Downloaded from https://chemistry-europe.onlinelibrary.wiley.com/doi/10.1002/cptc.70228 by Cochrane Croatia, Wiley Online Library on [24/11/2026]. See the Terms and Conditions (https://onlinelibrary.wiley.com/terms-and-conditions) on Wiley Online Library for rules of use; OA articles are governed by the applicable Creative Commons License

of these metalacyclic complexes, the central rhodium atom adopts a slightly distorted octahedral geometry as evident from the bond angles (Table 1). The five-membered metallacycles are planar and exhibit alternating carbon–carbon bond lengths, which is consistent with a rhodacyclopentadiene structure. The phosphine ligands in each of these complexes show a *trans*-disposition, and the Rh—P bond lengths observed in **3** and **4** are slightly shorter (*ca*. 0.05 Å) than that found in **2** indicating weaker metal-phosphine bonding in the latter, which is consistent with the σ-donating ability and steric bulk of the corresponding phosphine ligands. The overall structural features of **2**-**4** are also very similar to those of the other MC_4 rhodacyclopentadienes reported earlier by our group [43–48].

2.2 | Photophysical Studies

The linear optical properties of **3** and **4** are summarized in Table 2, and their absorption and emission spectra are displayed in Figures 2 and 3 (see also Supporting Information, Figures S10–S20). Compound **3a** displays intense absorptions in the UV–visible spectrum recorded in degassed toluene with peaks at 494 ($\varepsilon = 37\,600\ mol^{-1}\ cm^{-1}\ dm^3$), 462 ($\varepsilon = 38\,500\ mol^{-1}\ cm^{-1}\ dm^3$), and 307 nm ($\varepsilon = 34\,000\ mol^{-1}\ cm^{-1}\ dm^3$), and emits in the visible region with peaks at 509, 549, and 590 nm. The emission of **3a** is barely sensitive to solvent effects as it shows only a slight hypsochromic shift (116 cm^{-1}) in ethanol. We also note that the molar extinction coefficient decreases by a factor of two in ethanol as compared to toluene. Both the absorption and emission show a vibrational progression of approximately 1400 cm^{-1}. The photoluminescence quantum yield (Φ_{PL}) of **3a** was found to be ∼0 with a lifetime < 0.1 ns indicating the presence of very efficient nonradiative decay pathways. Compound **3b**, which is an isotopologue of **3a**, exhibits almost identical photophysical properties except that the values of the molar extinction coefficients are ca. 20% higher for **3b** as compared to **3a**. As the Φ_{PL} was found ∼0 for both isotopologues, evaluation of the involvement of C–H vibration of the methyl groups of the PMe_3 ligands in the nonradiative decay pathway of **3** is not possible.

Interestingly, related rhodacyclopentadienes bearing weaker donor groups, such as SMe and OMe, at the *para*-positions [44–47] tend to fluoresce significantly more efficiently. For example, Φ_{PL} values of up to 0.34 have been observed for related rhodacyclopentadienes containing SMe groups at the *para*-position

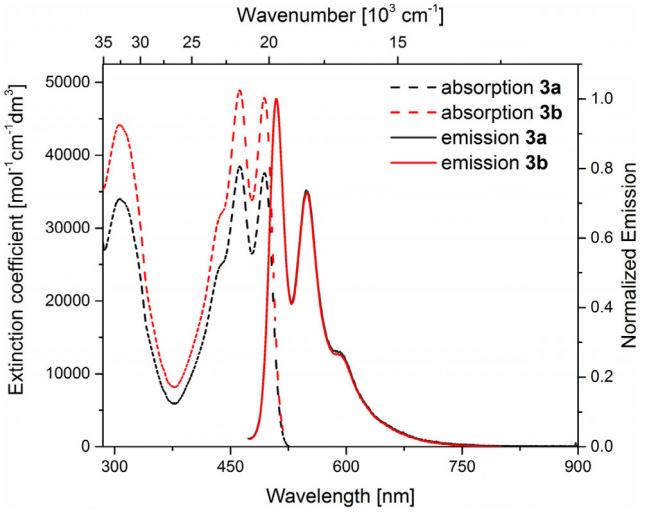

FIGURE 2 | Absorption (dashed line) and normalized emission (solid line) spectra of **3a** (black) and **3b** (red) recorded in degassed toluene at room temperature with excitation at 462 nm.

of the phenyl groups whereas strong acceptor substituents such as CO_2Me or $B(Mes)_2$ lead to much higher quantum yields of up to 69% [44, 45, 47]. We did not carry out further investigations to understand why the Φ_{PL} is negligible for these NMe_2-substituted rhodacyclopentadienes as it is not related to the aim of this work, which was the water-soluble dicationic complexes (**4**) in which the cationic NMe_3 groups serve as inductively withdrawing substituents rather than as strong π donors.

Thus, compound **4a** shows intense visible luminescence peaks at 540 and 580 nm (Figure 3) with $\Phi_{PL} = 0.33$ and an emission lifetime of 1.50 ns in ethanol (Table 2). The lowest energy absorption maximum was observed at 509 nm with a molar extinction coefficient of 31,900 $mol^{-1}cm^{-1}dm^3$. A vibrational progression of *ca*. 1275 cm^{-1} is observed in the absorption and emission spectra. The short emission lifetime (1.50 ns) and small Stokes shift (1128 cm^{-1}) observed in degassed ethanol at room temperature and the overlap of the excitation and emission spectra indicate that the observed luminescence is fluorescence from the S_1 state, similar to the related rhodacyclopentadienes reported earlier by our group which exhibit fluorescence but no observable phosphorescence [44–47]. The ISC process (from the S_1 to the T_1 state) is unusually slow in these rhodacyclopentadienes, occurring on

TABLE 2 | Selected photophysical data of compounds **3a**, **3b**, **4a**, and **4b** recorded under oxygen-free conditions at room temperature.

Compound	Medium	λ_{max} (abs), nm	ε, $mol^{-1}cm^{-1}dm^3$	λ_{max} (em), nm	Stokes shift, cm^{-1}	Φ_{PL}	τ_f, ns	Φ_Δ[a]
3a	Toluene	494	37,600	509	597	∼0	<0.1	
	Ethanol	489	18,500	506	687	∼0	<0.1	
3b	Toluene	494	47,900	509	597	∼0	<0.1	
	Ethanol	490	23,100	507	684	∼0	<0.1	
4a	Ethanol	509	31,900	540	1128	0.33	1.50	0.51
	Water	498	14,900	549	1865	0.03		
4b	Ethanol	509	31,100	540	1128	0.31	1.50	

[a]Quantum yield for O_2 ($^1\Delta_g$) formation in O_2 saturated solution.

23670932, 2026, 8, Downloaded from https://chemistry-europe.onlinelibrary.wiley.com/doi/10.1002/cptc.70228 by Cochrane Croatia, Wiley Online Library on [24/11/2026]. See the Terms and Conditions (https://onlinelibrary.wiley.com/terms-and-conditions) on Wiley Online Library for rules of use; OA articles are governed by the applicable Creative Commons License

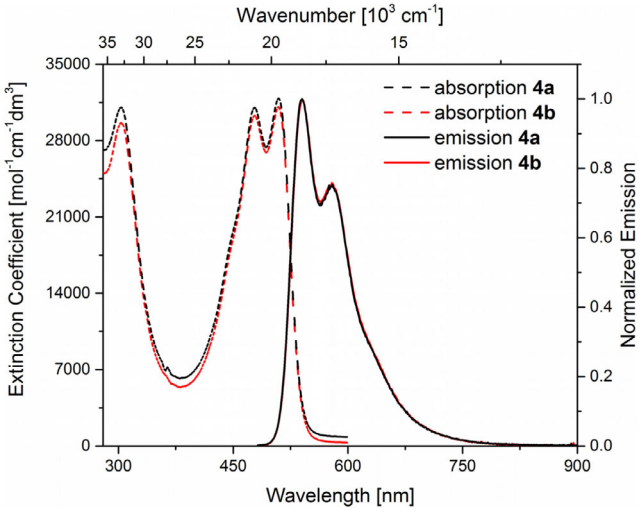

FIGURE 3 | Absorption (dashed line) and normalized emission (solid line) spectra of **4a** (black) and **4b** (red) recorded in degassed ethanol at room temperature with excitation at 478 nm.

the nanosecond timescale ($k_{ISC} = 10^8\ s^{-1}$), as deduced from our initial picosecond time-resolved transient IR measurements [44], mainly *via* a thermally activated ISC channel at temperatures above 233 K [45], while spin–orbit coupling (SOC)-based ISC occurs inefficiently at lower temperatures [45]. Our rhodacyclopentadienes were also found to act as potent sensitizers of singlet oxygen ($^1O_2$) and their quantum yields for $^1O_2$ generation in O_2-saturated solution indicate that $^1O_2$ formation occurs very efficiently from the T_1 state of these complexes. This assumption is also in accord with the fact that the intrinsic lifetimes of the S_1 states of these rhodacyclopentadienes are < 10 ns which is the minimum lifetime for an excited state to be able to generate $^1O_2$ considering a diffusion rate constant of *ca.* $10^{10}\ dm^3\ mol^{-1}\ s^{-1}$ and an oxygen concentration of *ca.* 10^{-3} mol dm^{-3} [44, 45]. The S_1 state with a relatively high fluorescence quantum yield observed for **4a** again leads us to conclude that the ISC from S_1 state to T_1 state in **4a** is also on the order of $10^8\ s^{-1}$. Singlet oxygen ($^1O_2$) sensitization of **4a** gave a quantum yield $\Phi_\Delta = 0.51$, indicating that photoexcited **4a** is a potent sensitizer of singlet oxygen. The fluorescence quantum yield ($\Phi_{PL} = 0.33$) and the quantum yield for $^1O_2$ formation in O_2-saturated solution ($\Phi_\Delta = 0.51$) observed for **4a** sum to close to unity indicating that there is very little nonradiative decay from either the S_1 or T_1 states, and the formation of $^1O_2$ from the T_1 state is very efficient.

Photosensitizers which generate singlet oxygen ($^1O_2$) upon light activation can damage targeted biomolecules such as cancer cells, and some are used for PDT [26]. However, high $^1O_2$ yields often lead to self-damage of the photosensitizer. Intense bubbling of air through an aqueous solution of **4a** under daylight led to slow decomposition (Supporting Information, Figure S3), which can be likely attributed to the photosensitizing properties of **4a**, as high singlet oxygen $^1O_2$ yields are often associated with self-sensitized degradation of the photosensitizer. Intensive $^1O_2$ production triggers type I and II reactions where the excited triplet photosensitizer reacts with $^1O_2$ or radicals, degrading the chromophore. This is common in many PDT candidates such as porphyrins and phthalocyanines, reducing efficacy over time as the agent deactivates before fully treating the target [50]. Of course, there are many strategies to address this issue. Thus, researchers optimize quantum yields, oxygen levels, and light doses to balance $^1O_2$ output without excess self-quenching. Aggregated or nanoparticle-encapsulated photosensitizers help localize $^1O_2$ near targets while minimizing self-exposure [51]. Notably, under ambient conditions at room temperature and daylight exposure, the UV/vis spectrum of **4a** remains essentially unchanged even after more than 24 h, allowing performance of biorelevant spectrometric studies (see Section: DNA/RNA and BSA Binding). In degassed water, **4a** shows minimal decomposition after 6 days (Supporting Information, Figure S4).

This behavior observed for our rhodacyclopentadienes is unusual, as one would typically expect very fast ISC, facilitated by the large SOC of a second-row transition metal like rhodium ($\xi = 1200\ cm^{-1}$), from the singlet state S_1 to the triplet state T_1 on the timescale of femto- to picoseconds (10^{-14}–10^{-10} s) [52–56], i.e., much faster than fluorescence. Consequently, either phosphorescence from the triplet state T_1 with lifetimes between micro- and milliseconds or nonradiative decay would be expected from metalacyclic complexes instead of fluorescence. Extensive theoretical calculations had been carried out which revealed that the following two factors are mainly responsible for the unusual "organic-like" photophysical behavior shown by these rhodacyclopentadienes: (i) The HOMO and LUMO are ligand-centered π and π* MOs due to the extended conjugation in the organic π-chromophore that not only lie in between the metal-centered filled and vacant orbitals but are also energetically well separated from them and (ii) the excited T_1 state exhibits structural distortion toward a cumulenic geometry, both features disfavoring coupling of the different spin states [45]. Very recently, we investigated, in more detail, the excited state properties of two related neutral rhodacyclopentadienes which contain either electron withdrawing —CO_2Me groups at the *para*-position of both phenyl groups or an electron donating NMe_2 group at one *para*-position and an electron withdrawing —CO_2Me group at the other *para*-position, using excitation-wavelength-dependent femtosecond transient absorption (fs-TA) spectroscopy and theoretical analysis [57]. This investigation confirmed that ISC in these rhodacyclopentadienes is dominated by the thermally activated $S_1 \rightarrow T_2$ channel, as the $S_1 \rightarrow T_1$ channel is blocked to a large extent by a high ISC barrier; however, the triplet state responsible for $^1O_2$ generation is the T_1 state due to rapid spin-allowed $T_2 \rightarrow T_1$ relaxation [57].

Compound **4a** also exhibits similar but poorly resolved absorption and emission spectra in water (Supporting Information, Figures S13 and S20). The absorption and emission spectra show small hypsochromic ($434\ cm^{-1}$) and bathochromic ($304\ cm^{-1}$) shifts, respectively, in water as compared to ethanol. However, a more profound impact of the solvent is observed for the photoluminescence quantum yield which decreased by an order of magnitude ($\Phi_{PL} = 0.03$ in water vs. 0.33 in EtOH).

The isotopologue of **4a**, i.e., compound **4b**, displays almost identical absorption and emission spectra with exactly the same emission lifetime (1.5 ns) in ethanol (Figure 3). The quantum yield of $\Phi_{PL} = 0.31$ measured for **4b** is also identical with that of **4a** within experimental error confirming that the C–H vibration of the methyl groups of PMe_3 ligand is not involved in the nonradiative decay pathways of **4**.

23670932, 2026, 8, Downloaded from https://chemistry-europe.onlinelibrary.wiley.com/doi/10.1002/cptc.70228 by Cochrane Croatia, Wiley Online Library on [24/11/2026]. See the Terms and Conditions (https://onlinelibrary.wiley.com/terms-and-conditions) on Wiley Online Library for rules of use; OA articles are governed by the applicable Creative Commons License

2.3 | DFT and TD-DFT Calculations

In order to validate that the same structural and electronic factors, as observed for the other similar fluorescent rhodacyclopentadienes reported previously by our group, are responsible for the origin of fluorescence despite the presence of a heavy metal atom, we carried out DFT and TD-DFT studies on **4a**. Details of the calculations are provided in the Supporting Information. The optimized ground-state (S_0) structure of **4a** shows excellent agreement with that determined by single crystal X-ray diffraction analysis. The bond lengths and bond angles involving the central rhodium atom are well-reproduced (Table 3). However, some deviations between computed and experimentally obtained dihedral angles are observed, likely due to crystal packing effects.

The frontier orbital region of the MO diagram of **4a** is shown in Figure 4. The HOMO and LUMO are energetically well-separated (4.73 eV) π-type ligand-based orbitals with very modest participation of the rhodium (*ca*. 7% in the HOMO and 1% in the LUMO). In addition, the energy difference between HOMO and HOMO-1 is 1.24 eV, while that between LUMO and LUMO + 1 is 1 eV indicating that both frontier orbitals are also somewhat isolated from the other occupied and vacant MOs. This energetically isolated state of HOMO and LUMO in **4a** can be explained by (i) the presence of an extended and highly conjugated π system that causes a small energy gap between the ligand-centered frontier orbitals and (ii) a large d-orbital splitting due to the presence of strong field ligands. The combined outcome of these two features disfavors interactions of the ligand-based frontier orbitals with the metal d orbitals due to increase in the energy difference and decrease in overlap between these orbitals, which was also the case for similar fluorescent rhodacyclopentadienes [45, 47]. This inhibits low-energy MLCT transitions, which could facilitate SOC and contribute to the nature of the emissive state, explaining the competitive fluorescence and ISC rate constants for **4a**.

TD-DFT calculations were also performed at different levels for **4a** to validate the experimentally observed main transitions including their percentage contributions to the excitations which are summarized in Table 4. The absorption maxima calculated using the PBE0/def2-svp functional and basis set match well with the absorption peaks found experimentally in ethanol (at 509, 478, 304, and 213 nm) although a vibrational progression was proposed to interpret the whole experimental UV–visible

TABLE 3 | Comparison of selected experimental and DFT-optimized structural parameters (PBE0 GD3BJ/def2-svp) of **4a**.[a]

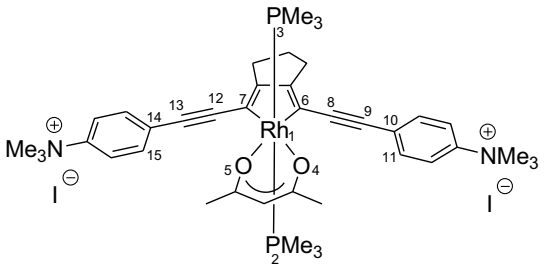

		Optimized geometry		
		In vacuum	Ethanol	X-ray geometry
Bond lengths, Å	Rh—P	2.3199	2.3210	2.2946
		2.3200	2.3211	2.3109
	Rh_1—C_6	2.0172	2.02012	2.029
	Rh_1—C_7	2.0178	2.02024	2.038
	Rh_1—O_4	2.1326	2.1338	2.133
	Rh_1—O_5	2.1329	2.1335	2.137
Bond angles, °	P_2—Rh_1—P_3	178.44	178.43	178.78
	C_6—Rh_1—C_7	81.11	81.14	80.82
	O_4—Rh_1—O_5	88.92	88.57	89.36
Dihedral angles, °	Rh_1—C_6—C_{10}—C_{11}	0.3764	4.7252	−2.1029
	Rh_1—C_7—C_{14}—C_{15}	3.4021	7.4339	−10.3560
	P_2—Rh_1—C_6—C_8	−91.4097	−89.8624	−81.2640
	P_2—Rh_1—C_7—C_{12}	91.2923	89.5237	76.3931
	P_3—Rh_1—C_6—C_8	89.4869	91.1324	99.9548
	P_3—Rh_1—C_6—C_8	−89.8257	−91.5230	−103.4819
	O_4—Rh_1—C_6—C_8	−2.5948	−1.0318	9.2575
	O_5—Rh_1—C_7—C_{12}	−0.9196	−2.5886	−14.1765

[a]Atom numbering for the participant atoms of the optimized structure follows the structure depicted below the table caption.

23670932, 2026, 8, Downloaded from https://chemistry-europe.onlinelibrary.wiley.com/doi/10.1002/cptc.70228 by Cochrane Croatia, Wiley Online Library on [24/11/2026]. See the Terms and Conditions (https://onlinelibrary.wiley.com/terms-and-conditions) on Wiley Online Library for rules of use; OA articles are governed by the applicable Creative Commons License

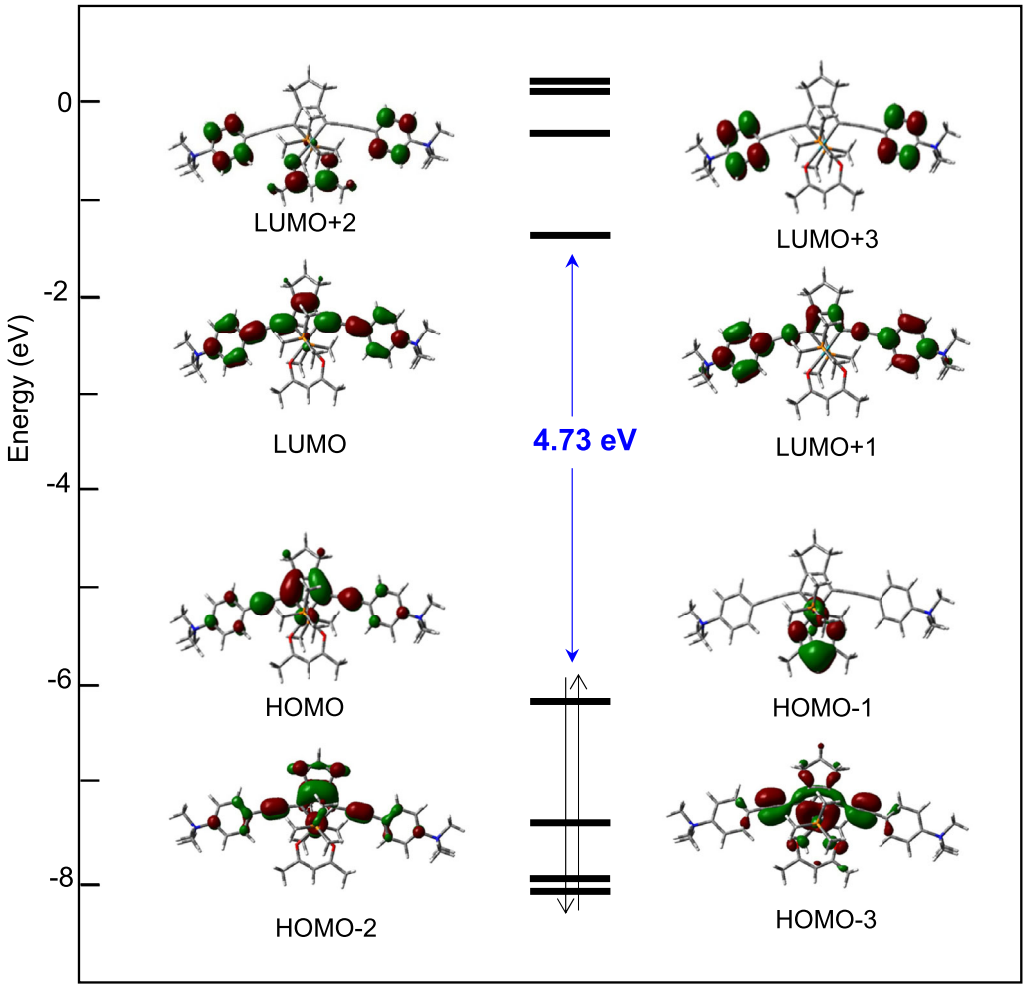

FIGURE 4 | CAM-B3LYP GD3BJ/def2-svp frontier MO diagram of **4a** in ethanol (isocontour values: 0.03 au).

TABLE 4 | Absorption wavelengths (λ_{calc}, nm), oscillator strengths (f), and main electronic transitions calculated for **4a** in ethanol. Corresponding excited state numbers (S_n) are given in brackets.

	λ_{exp}	λ_{calc}	f (S_n)	Main electronic transitions, weight %
PBE0 -GD3BJ/def2-svp	509, 478, 304, 213	546	1.11 (S_1)	H→L (98%)
		313	0.49 (S_5)	H-6→L (91%)
CAM-B3LYP GD3BJ/def2-svp		486	1.09 (S_1)	H→L (93%)
		272	0.73 (S_{15})	H-7→L (93%)
CAM-B3LYP GD3BJ/def2-tzvp		494	1.09 (S_1)	H→L (93%)
		296	0.032 (S_8)	H-5→L + 6 (48%); H-5→L (31%)

spectrum [58]. A better agreement with the experimental wavelengths was obtained using the CAM-B3LYP functional, which improved further when a more extended basis set such as the def2-tzvp was used. In all cases, the calculated low-energy absorption band corresponds to the $S_0 \rightarrow S_1$ transition and is the result of an electronic transition from the HOMO to the LUMO with an oscillator strength of $f > 1$. As stated earlier, both the HOMO and the LUMO are essentially π-type ligand-based orbitals and are well-separated in energy from lower-lying filled orbitals with significant metal contribution. Thus, the first excited state in **4a** correlates with a ligand-centered electronic transition (π–π*) which is common for fluorescent organic systems [59], but different from the majority of organometallic compounds that exhibit excited states with MLCT admixtures, which usually reduce the energy gap between S_1 and T_1 states in comparison with that for local (π–π*) excitations [60–62]. However, the calculated high-energy absorption band exhibits a large MLCT character as shown by the composition of the MOs involved in this transition [63].

2.4 | Two-Photon Absorption (TPA)

Two-photon absorption (TPA) is a photophysical process by which a molecule or material simultaneously absorbs a pair of

23670932, 2026, 8, Downloaded from https://chemistry-europe.onlinelibrary.wiley.com/doi/10.1002/cptc.70228 by Cochrane Croatia, Wiley Online Library on [24/11/2026]. See the Terms and Conditions (https://onlinelibrary.wiley.com/terms-and-conditions) on Wiley Online Library for rules of use; OA articles are governed by the applicable Creative Commons License

photons of the same or different energy via a virtual state. While one-photon absorption (OPA) is a linear process obeying the Beer–Lambert Law, TPA is a third-order nonlinear optical process and the energy absorbed through the latter process is quadratically proportional to the intensity of the incident light [64–68]. As the energy of the photons required for a typical TPA process is about half of the actual energy gap between the ground and excited states, low-energy photons having longer wavelengths, often in the near infrared (NIR), which is known as the biologically transparent window, are used for TPA which can penetrate deeper into the sample compared to higher-energy photons. This allows two-photon excitation to occur further inside a light-scattering medium which is useful for many applications including bioimaging [69–71]. Two-photon bioimaging also reduces the chance of photobleaching and photodamaging of imaging probes and cellular structures; hence, the use of two-photon microscopy in bioimaging is rapidly growing for the study of various dynamic biochemical processes in cells, thick tissues, and live animals [72]. Currently, only a few multiphoton fluorophores are commercially available, most of which are organic dyes, but the number of organic systems that can potentially be developed as multiphoton fluorophores is gradually increasing [70–78]. For example, we have reported two-photon bioimaging by a number of dipolar, quadrupolar, and octupolar triarylborane chromophores over the past few years [76–78]. Although quite a few metal complexes with TPA properties have been reported in recent years [30, 32–34, 79–84], few of those complexes have been used as two-photon fluorophores thus far [30, 32–34, 79]. Considering the many advantages of two-photon excited bioimaging over conventional one-photon chromophores, we examined the TPA properties of our water-soluble luminescent rhodacyclopentadiene **4a**.

As the polarity inside cells is more similar to polar organic solvents [83, 84], we measured the TPA spectrum of **4a** in EtOH, using the two-photon excited fluorescence technique, which is depicted in Figure 5 along with its OPA spectrum. The maximum of the TPA spectrum of **4a** showed a remarkable shift to shorter wavelength (higher energy), suggesting that TPA does not occur to the S_1 state, but instead, to a higher singlet state. Thus, a TPA maximum of ca. 290 GM is observed at ca. 680 nm.

These results demonstrate that, although the excitation wavelength of **4a** is not in the optimal bio-optical window ($\lambda_{exc} = 450–550$ nm), **4a** has applicable TPA properties with TPA absorption maximum at ca. 680 nm which would be appropriate for PDT and bioimaging applications [85, 86].

2.5 | DNA/RNA and BSA Binding

The dicationic complex **4a** was soluble in water up to $c = 5 \times 10^{-4}$ M. For more convenient spectrophotometric studies, a stock solution of $c = 2 \times 10^{-3}$ M was prepared in DMSO and diluted in aqueous medium prior to further experiments. The stock solution was stored at + 4 °C, being stable for a long period as demonstrated by UV/vis spectroscopy.

For more detailed characterization of its hydrophobic properties, we determined [87, 88] that $\log P_{ow} = 0.49$ (Supporting Information, Figure S45), defining complex **4a** as being slightly hydrophilic, fitting within the moderate log*P* range of −0.5 to 5, as per Lipinski's Rule of Five, and thus being a good candidate for passing biological membranes.

The absorbance of buffered solutions of the **4a** is proportional to concentration within the concentration range employed (Supporting Information, Figure S24). Upon increasing the temperature to 95 °C, changes in the UV/vis spectra were observed; thus, the absorbance decreases and, upon cooling to 25 °C, the

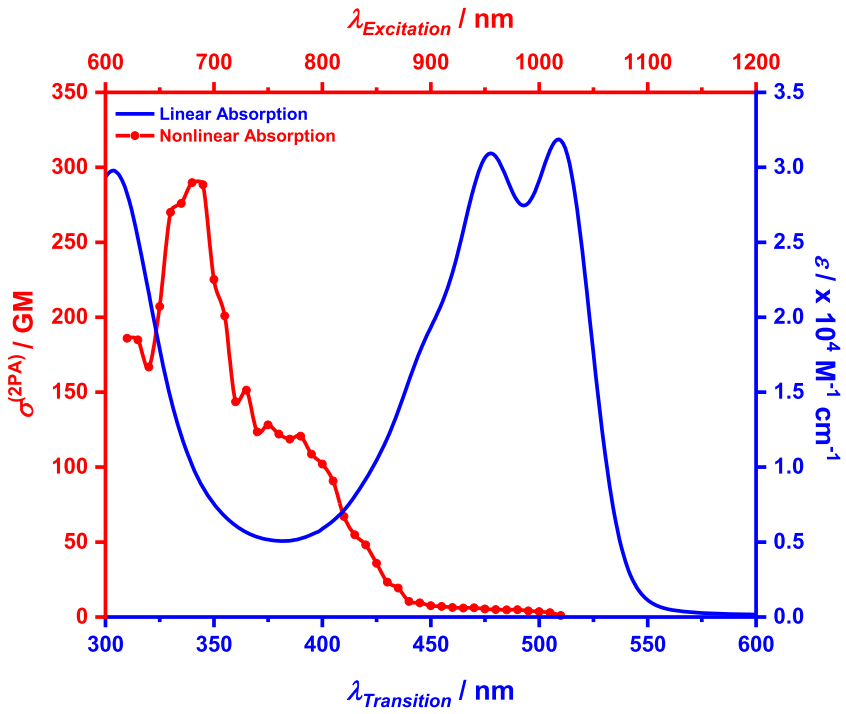

FIGURE 5 | One-photon absorption (blue) and two-photon absorption (red) spectra of **4a** in EtOH.

23670932, 2026, 8, Downloaded from https://chemistry-europe.onlinelibrary.wiley.com/doi/10.1002/cptc.70228 by Cochrane Croatia, Wiley Online Library on [24/11/2026]. See the Terms and Conditions (https://onlinelibrary.wiley.com/terms-and-conditions) on Wiley Online Library for rules of use; OA articles are governed by the applicable Creative Commons License

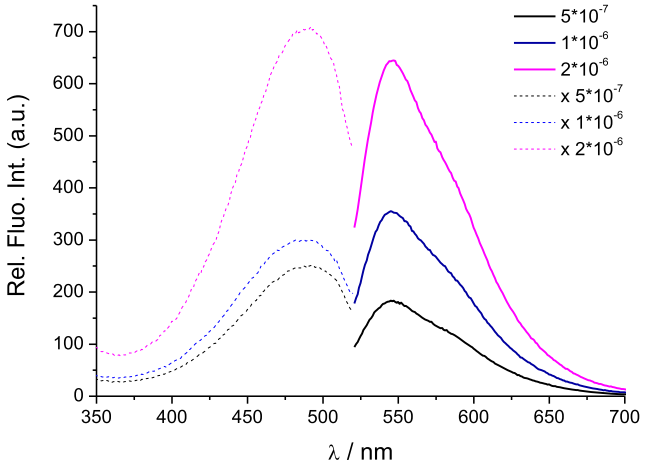

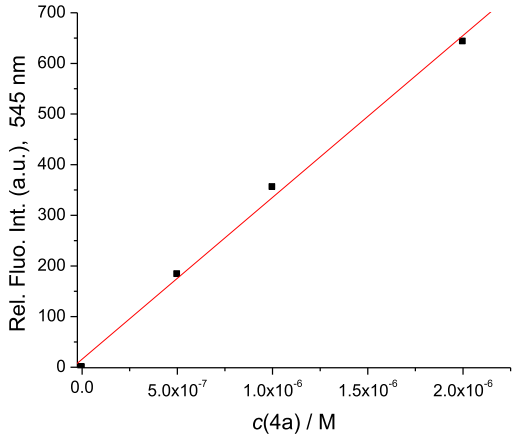

FIGURE 6 | Dependence of fluorescence excitation (- - -) and emission (—) spectra on the concentration of **4a**; $l_{exc} = 475$ nm and $l_{em} = 545$ nm. Done at pH 7.0, in sodium cacodylate buffer, $I = 50$ mM.

original spectrum was not recovered (Supporting Information, Figure S25), suggesting a permanent change in the compound structure, an important issue when discussing the thermal denaturation of ds-DNA/RNA. Complex **4a** exhibited rather weak emission in aqueous solution, being proportional to concentration within the μM range, and was stable over a long period, with the excitation spectrum matching the UV/vis spectrum (Figure 6).

Addition of ds-DNA or ds-RNA caused a measurable hypochromic effect on the UV/vis spectrum of **4a** (Supporting Information, Figures S26–S29), a well-established spectroscopic signature of small molecule DNA binding, particularly for groove binders. For example, well-known DNA minor groove binders, netropsin, distamycin, and Hoechst 33258, exhibit absorption hypochromism without significant hypsochromic or bathochromic shift [89]. This allowed collection of 7–9 titration data points, which enabled estimation of binding constants (Figure 7, logK_s 6–7) by means nonlinear fitting to the Scatchard equation (Supporting information) [90–92].

The strong emission of **4a** was efficiently quenched by ds-DNA/RNA, which allowed collection of a large number of data points in titrations (Figure 8a, Supporting Information Figures S30–S33).

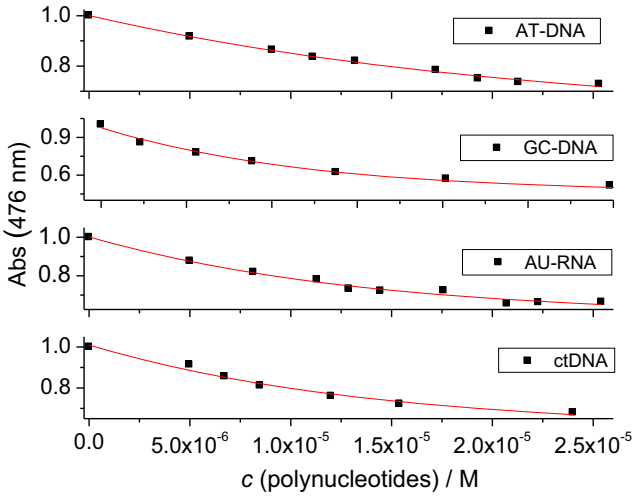

FIGURE 7 | Changes in the absorbance of **4a** ($c = 5 \times 10^{-6}$ M) upon addition of polynucleotides. Done at pH 7.0, in sodium cacodylate buffer, $I = 50$ mM.

The analysis of the titration data by means of the Scatchard equation [90–92] yielded the binding constants (Table 5), in good agreement with the binding constants estimated from UV/vis titrations. Detailed analysis of binding parameters showed that **4a** has no significant selectivity on binding affinity (Table 5), based on its fluorimetric response (Figure 8a), between various ds-DNAs or ds-RNA. Very intriguingly, the emission of **4a** was also efficiently quenched by addition of ss-polynucleotides (Supporting Information, Figures S34–S38), yielding binding constants comparable or even higher than those determined for ds-DNA or ds-RNA, which is not common for small, DNA/RNA-binding molecules [89]. Thus, small molecules typically bind to ds-DNA/RNA grooves (which ss-RNA does not have) or intercalate between ds-DNA/RNA base pairs (stabilized by aromatic stacking interactions between molecule and adjacent base pairs, whereby stacking is much weaker with ss-RNA single bases). Such unusually high affinity of **4a** toward ss-RNA required additional thermal denaturation experiments, presented in the section below (thermal denaturation experiments with ds-DNA and ds-RNA).

Intrigued by such broad binding affinity of **4a**, we also performed a titration with the protein BSA, which resulted in a strong emission increase from **4a** (Figure 8b), accompanied with similar binding affinity as for ds-DNA/RNA (Table 5). Thus, **4a** gives an opposite fluorimetric response for ds-DNA/RNA vs. BSA (Figure 8b) and can therefore be considered to be a strongly selective fluorimetric probe for proteins, with respect to any ds-DNA or ds-RNA.

2.6 | Thermal Denaturation Experiments with Ds-DNA and Ds-RNA

The thermal denaturation experiments provide information about the ds-polynucleotide helix thermal stability as a function of interaction with added small molecules [93]. The difference between the T_m value for the free ds-polynucleotide and that of a complex with a small molecule (ΔT_m value) is an important

23670932, 2026, 8, Downloaded from https://chemistry-europe.onlinelibrary.wiley.com/doi/10.1002/cptc.70228 by Cochrane Croatia, Wiley Online Library on [24/11/2026]. See the Terms and Conditions (https://onlinelibrary.wiley.com/terms-and-conditions) on Wiley Online Library for rules of use; OA articles are governed by the applicable Creative Commons License

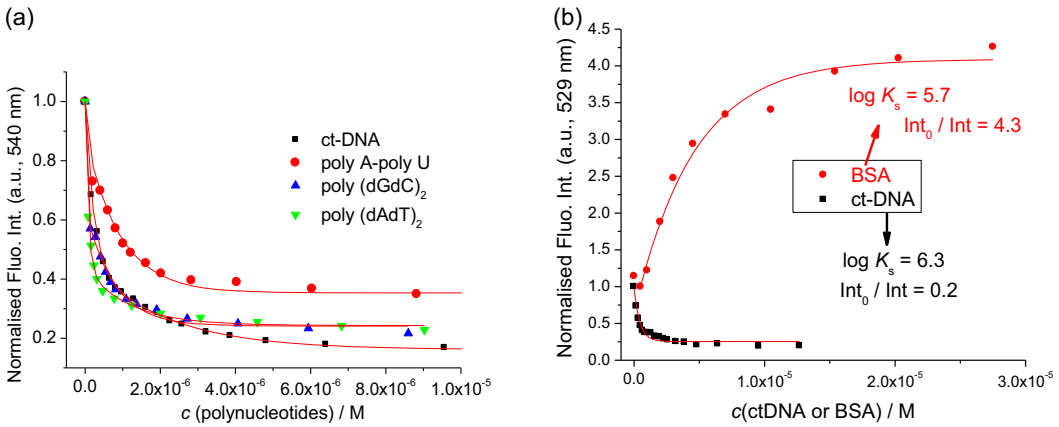

FIGURE 8 | (a) Changes in fluorescence intensity of **4a** ($c = 5 \times 10^{-7}$ M) upon addition of ds-polynucleotides at pH 7.0. Red lines denote fitting of the experimental data to the Scatchard equation [90–92]. (b) Changes in the fluorescence spectrum of **4a** ($c = 5.0 \times 10^{-7}$ M, $l_{exc} = 475$ nm) upon titration with ct-DNA or BSA. Done at pH 7.0, in sodium cacodylate buffer, $I = 0.05$ M. Red lines denote fitting of experimental data to the Scatchard equation [90–92] for ct-DNA and fitting of experimental data to a 1:1 stoichiometry complex formed for BSA.

TABLE 5 | Binding constants[a,b] (logK_s) of complexes **4a** with ds- and ss-polynucleotides calculated by processing fluorimetric titrations at pH = 7.0, sodium cacodylate buffer, $I = 0.05$ M.

ds-DNA			ds-RNA	ss-RNA				
ct-DNA	**poly(dGdC)$_2$**	**poly(dAdT)$_2$**	**polyA-polyU**	**polyA**	**polyU**	**polyG**	**polyC**	**[b]BSA**
6.3	6.5	6.8	6.1	6.6	6.8	6.4	7.0	5.7

[a]Processing of the titration data by means of the Scatchard equation [90–92] gave values of the ratio n[bound **4a**]/[polynucleotide] = 0.1– 0.3 for ds-DNA/RNA and ca. $n = 0.5$–1 for ss-RNA; for easier comparison, all log*Ks* values were re-calculated for fixed $n = 0.2$ (ds-DNA/RNA) and $n = 0.5$ (ss-RNA). Correlation coefficients were > 0.99 for all calculated *Ks* values.
[b]Titration of **4a** with BSA gave best fit for 1:1 stoichiometry of **4a**/BSA complex, giving binding constant logK_s.

factor in the characterization of small molecule/ds-polynucleotide interactions. For example, moderate to strong stabilization ($\Delta T_m > 5$ °C) supports pronounced intercalative or minor groove binding interaction [89], whereas weak or negligible stabilization ($\Delta T_m = 0$–5 °C) suggests a binding process driven mostly by the hydrophobic effect accompanied by weak H-bonding and/or electrostatic interactions, usually excluding classical intercalation as a binding mode. Furthermore, negative ΔT_m values suggest destabilization of ds-polynucleotide, which can be caused by higher affinity toward ss-polynucleotides, or promoted formation of poly-stranded DNA/RNA structures [89].

Thermal denaturation experiments showed very unusual destabilization of ds-DNA or ds-RNA by added **4a** (Table 6, Supporting Information, Figures S39–S41). However, as noted above in the discussion of UV/vis spectra, complex **4a** decomposes at increased temperatures (Figure S25); thus, it is not clear whether such a process can produce reactive species, which interact with ds-DNA/RNA and destabilize the helices against thermal denaturation.

TABLE 6 | ΔT_m-Values[a] (°C) for different ratios [b]*r* of **4a** added to polynucleotide.

r	ct-DNA	p(dAdT)$_2$	polyA-polyU
0.2	−3.0	—	—
0.3	−5.0	0	−8.0

[a]ΔT_m- Values.
[b]r = [**4a**]/[polynucleotide].

Also, as evident from the results in Table 5, the affinity of **4a** toward some ss-RNAs is higher in comparison to those with ds-RNA or ds-DNA. For example, binding constants for poly U (log$K_s = 6.8$) or for poly A (log$K_s = 6.6$) are almost an order of magnitude higher in comparison to that for double-stranded poly A - poly U (log$K_s = 6.1$). In the process of thermal denaturation, double-stranded RNA is systematically unwound, exposing ss-regions for **4a** high-affinity binding, and in that way, complex **4a** promotes double-strand decomposition and generally lowers the melting point of ds-RNA. The same is valid for the G-C sequence in ct-DNA (in comparison to poly G and poly C), consequently causing minor destabilization of ct-DNA. However, it does not hold for p(dAdT)$_2$, for which **4a** has the highest binding constant (Table 5) and, therefore, no destabilization effect was observed (Table 6). Our results support the binding of **4a** within the ds-DNA minor groove, which in p(dAdT)$_2$ is best suited for small molecule binding [89, 94].

2.7 | Circular Dichroism (CD) Experiments

To investigate the binding of **4a** to ds-DNA/RNA and ss-polynucleotides in more structural detail, we used circular dichroism (CD) spectroscopy. CD spectroscopy is a useful analytical tool to study the binding of small molecules to chiral macromolecules such as DNA [95], as it can provide information on the mode of binding to the polynucleotide, with distinctive spectral differences for intercalators and groove binding derivatives [96–98].

23670932, 2026, 8, Downloaded from https://chemistry-europe.onlinelibrary.wiley.com/doi/10.1002/cptc.70228 by Cochrane Croatia, Wiley Online Library on [24/11/2026]. See the Terms and Conditions (https://onlinelibrary.wiley.com/terms-and-conditions) on Wiley Online Library for rules of use; OA articles are governed by the applicable Creative Commons License

Complex **4a** itself is not chiral, thus not interfering with monitoring of the CD spectral properties of DNA/RNA.

Addition of **4a** strongly decreased the CD spectrum (220–300 nm) of AT-DNA (Supporting Information, Figure S42), induced smaller changes in the CD spectra of mixed sequence ct-DNA, and led to negligible changes of the spectra of GC-DNA and AU-RNA. Such AT-DNA-directed selectivity strongly supports binding in the AT-DNA minor groove [96–98]. Furthermore, addition of **4a** induced a moderate decrease in CD spectra of ss-polynucleotides (Supporting Information, Figure S43), supporting formation of a **4a** /ss–RNA complex under biorelevant conditions, in line with fluorimetric titrations (Table 5, Supporting Information, Figure S38).

To provide additional information regarding the binding site of **4a**, we performed a competition experiment with well-known AT-DNA groove binder DAPI, based on its strong positive ICD band at 380 nm [97, 99]. Indeed, addition of **4a** significantly decreased the ICD band of DAPI/DNA complex (Supporting Information, Figure S44), reaching a 50% decrease at a ratio of r[**4a**]/[DAPI] = 2, further additions of **4a** causing the colloidization of a sample, which prevented collection of accurate CD spectra. The results obtained, showing approximately 50% of DAPI displacement at a ratio of r[**4a**]/[DAPI] = 2, suggest an order of magnitude stronger binding of DAPI with respect to **4a**, which is in accordance with determined binding constant (Table 5) with respect to the DAPI binding constant for AT-DNA which is within the $K_s = 10^7$–$10^8\ M^{-1}$ range [99–101].

2.8 | Cell Cytotoxicity and Live-Cell Imaging

The water stability of **4a** together with its suitable photophysical properties mentioned above makes it a promising candidate for live-cell imaging which prompted us to investigate its possible cytotoxicity in cells. Thus, we exposed two different cell lines, A549 tumor cell and WI38 normal human cell, to solutions containing varying amounts of **4a**, and studied the cell metabolic activity with a colorimetric (MTT) assay after 96 h. These studies showed that **4a** has no cytotoxic effect at concentrations as high as 10 μM, even upon irradiation by visible light (Figure 9), and thus can be safely used for live-cell imaging.

Next, we treated living A549 cells with a 10 μM concentration of **4a** and performed confocal laser scanning fluorescence microscopy taking advantage of the fluorescence shown by our dye. Confocal microscopy showed that **4a** successfully enters cells within 90 min of incubation at 37 °C. We also observed strong selectivity (>90%) of **4a** to accumulate in mitochondria which was confirmed by co-localization experiments using the commercial mitochondrial imaging agent MitoTracker Red (Figure 10).

Furthermore, we have also analyzed, in detail, fluorescence from **4a** inside cells (mitochondria) by collecting the emission spectrum in the 500–600 nm range (Figure 11). Comparison of the spectrum (Figure 11, top left) with previously performed titrations with DNA or BSA (Figure 8b, Figure 11, bottom left)

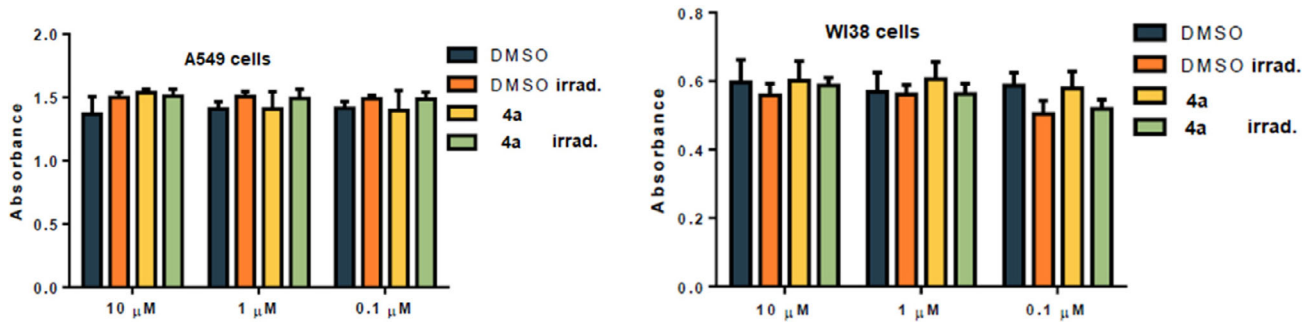

FIGURE 9 | Cell survival of A549 (top) and WI38 (bottom) cells exposed to **4a**. Data denoted as "irrad" represent cells irradiated by visible light (eight overhead-mounted LZC-420 lamps, in total 64 W, wavelength range 400–700 nm) for 30 min periods, each of 3 days of cell incubation during the MTT procedure. Data are presented as mean ± SD from four replicates, relative to the control samples. Control samples are cells treated with DMSO in the same concentration as that of the compound tested. Representative data of three independent experiments which yielded similar results are shown.

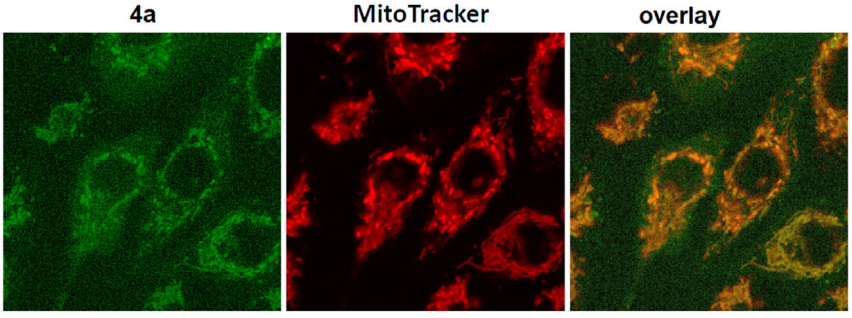

FIGURE 10 | Uptake and localization of **4a** (10 μM) in living A549 cells. Cells were treated with **4a** for 90 min at 37 °C, the surplus dye being washed out with cell culture medium, and subsequently observed by confocal microscopy, $\lambda_{exc} = 457$ nm, $\lambda_{em} = 500$–600 nm. Co-localization with MitoTracker ($\lambda_{exc} = 644$ nm, $\lambda_{em} = 665$ nm). A Pearson's coefficient of > 0.9 denoted excellent co-localization of the two dyes.

23670932, 2026, 8, Downloaded from https://chemistry-europe.onlinelibrary.wiley.com/doi/10.1002/cptc.70228 by Cochrane Croatia, Wiley Online Library on [24/11/2026]. See the Terms and Conditions (https://onlinelibrary.wiley.com/terms-and-conditions) on Wiley Online Library for rules of use; OA articles are governed by the applicable Creative Commons License

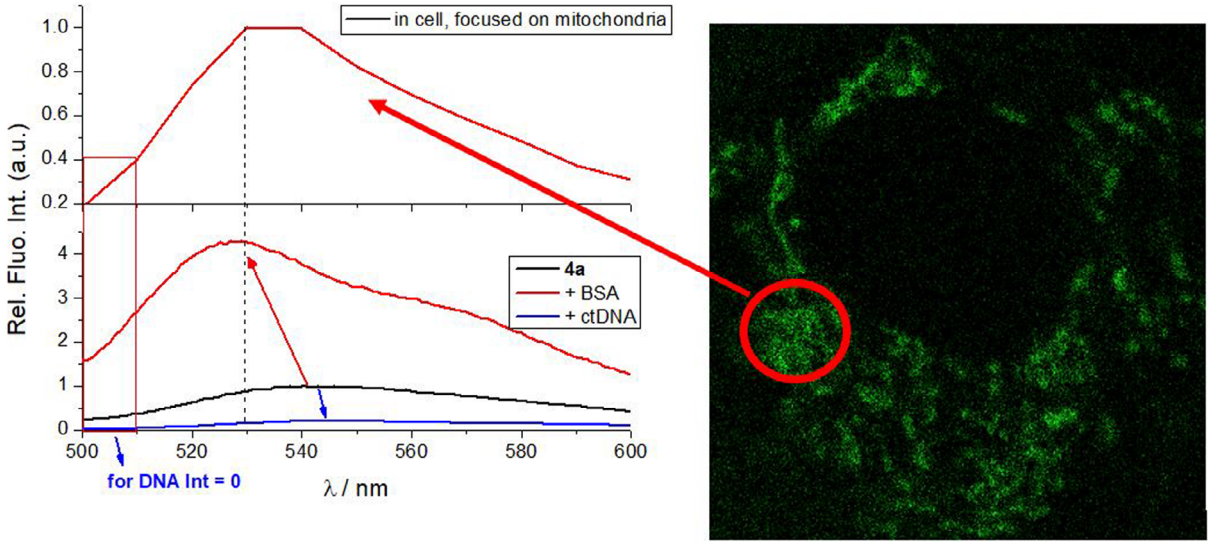

FIGURE 11 | Right: Uptake and localization of **4a** (10 μM) in live A549 cells, treated with **4a** for 90 min at 37 °C (the surplus of dye having been washed out with buffer) and subsequently observed by confocal microscopy, $\lambda_{exc} = 457$ nm, $\lambda_{em} = 500–600$ nm (top left). The microscope was then focused on the mitochondria area (marked with a red circle), and the emission spectrum was collected in the 500–600 nm range, with 10 nm resolution. Lower left: **4a** emission spectra collected in a cuvette upon titration with DNA or BSA for comparison (see Figure 4). Note that at 510 nm, the emission intensity of the **4a**/DNA complex is zero.

strongly supports binding of **4a** within the mitochondrial membranes and not interacting with mitochondrial DNA.

Furthermore, on the confocal microscope, we irradiated **4a**-treated (10 μM) live A549 cells with the full power of the 457 nm laser and monitored changes in the cells (Supporting Information, Movie S1). No apparent effect on cell morphology was observed, in line with prior observed nontoxicity (Figure 9); however, strong and very rapid bleaching of the **4a** emission suggested photoinduced dye decomposition. It seems that, although **4a** is efficient singlet oxygen sensitizer in a cuvette, it photochemically decomposes quite rapidly inside cells under high-power light irradiation; however, its localization in the mitochondrial membrane does not lead to significant damage, as demonstrated by its negligible cytotoxic effect. This seemingly kinetically controlled process suggests the necessity of optimization by structural modification of **4a**; thus, new analogs should be designed and tested. Interestingly, however, whatever the "decomposition" process is, it does not lead to the release of substances which are toxic to the cells.

3 | Conclusions

We have synthesized a water-soluble 2,5-bis(arylethynyl)rhodacyclopentadiene (**4a**) which exhibits fluorescence from the S_1 excited state in both organic and aqueous solutions, but no observable phosphorescence from T_1 at room temperature that normally would have been expected for octahedral organometallic complex bearing a second-row transition metal. The $S_1 \rightarrow T_1$ ISC in **4a** is unusually slow, and singlet oxygen ($^1O_2$) sensitization experiments were carried out to estimate the quantum yield for ISC indirectly. The Φ_Δ value of 0.51 obtained from this experiment indicates that **4a** can act as a potent sensitizer of $^1O_2$ as the formation of $^1O_2$ from the T_1 state is very efficient. DFT and TD-DFT studies reveal that the frontier MOs of **4a** are nearly pure ligand-based π-type MOs with very modest contributions from the rhodium due to the presence of highly conjugated organic π-chromophore, and both the HOMO and LUMO are also somewhat isolated from the metal-centered filled and vacant orbitals. These features hinder the ISC process; thus, the ISC is unusually slow in **4a** which leads to the observation of competitive fluorescence and triplet state formation, typical of this class of rhodacyclopentadienes. Complex **4b** which is an isotopologue of **4a** was also synthesized by replacing the PMe_3 ligands with $P(CD_3)_3$ in order to shed light on the nonradiative decay process of **4**. The values of photoluminescent quantum yield and lifetime were identical within experimental error for both isotopologues confirming that C—H vibrations of the methyl groups of the PMe_3 ligands are not involved in the nonradiative decay pathways of **4**. A reasonably large TPA cross-section ca. 290 GM was observed at ca. 680 nm.

Biological studies reveal that **4a** does not show any significant selectivity between various ds-DNAs or ds-RNA. However, the dye can be used as a specific fluorimetric probe as its emission is strongly enhanced only for protein (BSA) in contrast to efficient quenching by DNA/RNA. This selective response can eventually be used for the recognition of the **4a**/BSA complex by its strong fluorescence increase with respect to the eventual binding of **4a** to fragmented, "free-floating" cell-free DNA (cfDNA), in the bloodstream, causing strong quenching of emission. Further studies indicated that **4a** binds within the ds-DNA minor groove which, in $p(dAdT)_2$, is best suited for small molecule binding. Intriguingly, **4a** shows stronger affinity toward ss-RNA with respect to ds-RNA, which is one of the causes for thermal destabilization of the ds-RNA helix, which is quite unusual for small molecule interactions with nucleic acids [89]. Detailed structural studies by NMR would be needed to understand the precise mechanism of such ss-RNA selectivity.

23670932, 2026, 8, Downloaded from https://chemistry-europe.onlinelibrary.wiley.com/doi/10.1002/cptc.70228 by Cochrane Croatia, Wiley Online Library on [24/11/2026]. See the Terms and Conditions (https://onlinelibrary.wiley.com/terms-and-conditions) on Wiley Online Library for rules of use; OA articles are governed by the applicable Creative Commons License

As far as we are aware, only two luminescent rhodium complexes have been employed in cell imaging thus far [102]. The core of both these complexes consists of two 2-phenylpyridyl ligands and a 2,2′-bipyridine ligand, $[Rh(C–N)_2(N–N)]^+$, functionalized with either biotin or an ethyl unit. However, no specific targeting was observed, as both display perinuclear staining and negligible nuclear accumulation, although one of them was bio-conjugated with biotin. In contrast, complex **4a** efficiently enters living human cells and accumulates selectively in mitochondrial membranes, being nontoxic even at high (10 μM) concentrations. Although **4a** is a potent sensitizer of singlet oxygen ($^1O_2$) in a cuvette, exposure of the dye accumulated inside human cells to intense visible light results in fast bleaching of **4a** with no effect on cell viability, thus suggesting local consumption of $^1O_2$ by dye decomposition. The one-photon excitation wavelength of **4a** is not in the optimal bio-optical window ($\lambda_{exc} > 600$ nm); however, we showed that **4a** has applicable TPA properties, which supports the further development of analogs of this dye, including optimization of bleaching properties and photoactivity in living cells.

3.1 | Crystal Structures

Deposition Numbers 2079219 (**2**), 2072536 (**3a**), 2072537 (**3b**), 2072538 (**4a**), and 2072539 (**4b**) contain the supplementary crystallographic data for this paper. These data are provided free of charge by the joint Cambridge Crystallographic Data Centre and Fachinformationszentrum Karlsruhe Access Structures service.

Author Contributions

T.B.M., S.G., and I.P. conceived the idea. S.G., T.G., and S.L. conducted the synthesis and characterization of the compounds. A.A., J.N., A.B., and J.-F.H. performed the computational studies. S.G., F.K., and J.N. conducted photophysical experiments. E.M. conducted the two-photon absorption study. A.F. conducted the X-ray crystallographic studies. M.J. and K.B. conducted the bioimaging and biomolecule sensing experiments. S.G., T.B.M., and I.P. wrote the first draft. T.B.M., C.L., and I.P. supervised the research groups, assisted in the analysis of all data, and revised the manuscript. All authors have read and agreed to the published version of the manuscript.

Acknowledgments

S.G. thanks the Alexander von Humboldt Foundation for the award of a postdoctoral fellowship. T.B.M. thanks the Julius-Maximilians-Universität Würzburg for support.

Funding

This work was supported by the Alexander von Humboldt Foundation, Julius-Maximilians-Universität Würzburg and Croatian Science Foundation under the project number HrZZ IP-2022-10-9829.

Conflicts of Interest

The authors declare no conflicts of interest.

Data Availability Statement

The data that support the findings of this study are available in the Supporting Information of this article.

References

1. E. Baggaley, J. A. Weinstein, and J. A. G. Williams, "Lighting the Way to See inside the Live Cell with Luminescent Transition Metal Complexes," *Coordination Chemistry Reviews* 256 (2012): 1762–1785.

2. H. F. Xiang, J. H. Cheng, X. F. Ma, X. G. Zhou, and J. J. Chruma, "Near-Infrared Phosphorescence: Materials and Applications," *Chemical Society Reviews* 42 (2013): 6128–6185.

3. V. Fernández-Moreira, F. L. Thorp-Greenwood, and M. P. Coogan, "Application of d6 Transition Metal Complexes in Fluorescence Cell Imaging," *Chemical Communications* 46 (2010): 186–202.

4. D.-L. Ma, H.-Z. He, D. S.-H. Chan, and C.-H. Leung, "Bioactive Luminescent Transition-Metal Complexes for Biomedical Applications," *Angewandte Chemie International Edition* 52 (2013): 7666–7682.

5. M. P. Coogan and V. Fernández-Moreira, "Progress with, and Prospects for, Metal Complexes in Cell Imaging," *Chemical Communications* 50 (2014): 384–399.

6. Y. You and W. Nam, "Photofunctional Triplet Excited States of Cyclometalated Ir(III) Complexes: Beyond Electroluminescence," *Chemical Society Reviews* 41 (2012): 7061–7084.

7. K. K.-W. Lo and K. Y. Zhang, "Iridium(iii) Complexes as Therapeutic and Bioimaging Reagents for Cellular Applications," *RSC Advances* 2 (2012): 12069–12083.

8. K. K.-W. Lo, K. Y. Zhang, and S. P.-Y. Li, "Design of Cyclometalated Iridium(III) Polypyridine Complexes as Luminescent Biological Labels and Probes," *Pure and Applied Chemistry* 83 (2011): 823–840.

9. K. K.-W. Lo, S. P.-Y. Li, and K. Y. Zhang, "Development of Luminescent Iridium(III) Polypyridine Complexes as Chemical and Biological Probes," *New Journal of Chemistry* 35 (2011): 265–287.

10. C. Ulbricht, B. Beyer, C. Friebe, A. Winter, and U. S. Schubert, "Recent Developments in the Application of Phosphorescent Iridium(III) Complex Systems," *Advanced Materials (Deerfield Beach, Fla.)* 21 (2009): 4418–4441.

11. K. K.-W. Lo, M.-W. Louie, and K. Y. Zhang, "Design of Luminescent Iridium(III) and Rhenium(I) Polypyridine Complexes as In Vitro and In Vivo Ion, Molecular and Biological Probes," *Coordination Chemistry Reviews* 254 (2010): 2603–2622.

12. K. K.-W. Lo, M.-W. Louie, K. Y. Zhang, and S. P.-Y. Li, "Recent Exploitation of Luminescent Rhenium(I) Tricarbonyl Polypyridine Complexes as Biomolecular and Cellular Probes," *European Journal of Inorganic Chemistry* 2011 (2011): 3551–3568.

13. M. R. Gill and J. A. Thomas, "Ruthenium(II) Polypyridyl Complexes and DNA—From Structural Probes to Cellular Imaging and Therapeutics," *Chemical Society Reviews* 41 (2012): 3179–3192.

14. A. M. Paoletti, G. Pennesi, G. Rossi, A. Generosi, B. Paci, and V. R. Albertini, "Titanium and Ruthenium Phthalocyanines for NO_2 Sensors: A Mini-Review," *Sensors* 9 (2009): 5277–5297.

15. F. L. Thorp-Greenwood, "An Introduction to Organometallic Complexes in Fluorescence Cell Imaging: Current Applications and Future Prospects," *Organometallics* 31 (2012): 5686–5692.

16. F. L. Thorp-Greenwood, R. G. Balasingham, and M. P. Coogan, "Organometallic Complexes of Transition Metals in Luminescent Cell Imaging Applications," *Journal of Organometallic Chemistry* 714 (2012): 12–21.

17. K. K.-W. Lo, A. W.-T. Choi, and W. H.-T. Law, "Applications of Luminescent Inorganic and Organometallic Transition Metal Complexes as Biomolecular and Cellular Probes," *Dalton Transactions* 41 (2012): 6021–6047.

18. M. Para and G. Gasser, "Organometallic Compounds: An Opportunity for Chemical Biology?," *ChemBioChem* 13 (2012): 1232–1252.

19. Y. Ma and Y. Wang, "Recent Advances in the Sensitized Luminescence of Organic Europium Complexes," *Coordination Chemistry Reviews* 254 (2010): 972–990.

23670932, 2026, 8, Downloaded from https://chemistry-europe.onlinelibrary.wiley.com/doi/10.1002/cptc.70228 by Cochrane Croatia, Wiley Online Library on [24/11/2026]. See the Terms and Conditions (https://onlinelibrary.wiley.com/terms-and-conditions) on Wiley Online Library for rules of use; OA articles are governed by the applicable Creative Commons License

20. J.-C. Bünzli, "Lanthanide Luminescence for Biomedical Analyses and Imaging," *Chemical Reviews* 110 (2010): 2729–2755.

21. J.-C. G. Bunzli and S. V. Eliseeva, "Intriguing Aspects of Lanthanide Luminescence," *Chemical Science* 4 (2013): 1939–1949.

22. L. J. Charbonniere, "Luminescent Lanthanide Labels," *Current Inorganic Chemistrye* 1 (2011): 2–16.

23. E. J. New, D. Parker, D. G. Smith, and J. W. Walton, "Development of Responsive Lanthanide Probes for Cellular Applications," *Current Opinion in Chemical Biology* 14 (2010): 238–246.

24. D. Parker, "Critical Design Factors for Optical Imaging with Metal Coordination Complexes," *Australian Journal of Chemistry* 64 (2011): 239–243.

25. A. Ruggi, F. W. B. van Leeuwen, and A. H. Velders, "Interaction of Dioxygen with the Electronic Excited State of Ir(III) and Ru(II) Complexes: Principles and Biomedical Applications," *Coordination Chemistry Reviews* 255 (2011): 2542–2554.

26. D. Phillips, "Toward Targeted Photodynamic Therapy," *Pure and Applied Chemistry* 83 (2011): 733–748.

27. J. Funkhouser, "Reinventing Pharma: The Theranostic Revolution," *Current Drug Discovery* 2 (2002): 17–19.

28. L. Murphy, A. Congreve, L.-O. Pålsson, and J. A. G. Williams, "The Time Domain in Co-Stained Cell Imaging: Time-Resolved Emission Imaging Microscopy Using a Protonatable Luminescent Iridium Complex," *Chemical Communications* 46 (2010): 8743–8745.

29. K. Y. Zhang, S. P.-Y. Li, N. Zhu, et al., "Structure, Photophysical and Electrochemical Properties, Biomolecular Interactions, and Intracellular Uptake of Luminescent Cyclometalated Iridium(III) Dipyridoquinoxaline Complexes," *Inorganic Chemistry* 49 (2010): 2530–2540.

30. S. W. Botchway, M. Charnley, J. W. Haycock, et al., "Time-Resolved and Two-Photon Emission Imaging Microscopy of Live Cells with Inert Platinum Complexes," *Proceedings of the National Academy of Sciences* 105 (2008): 16071–16076.

31. P. Wu, E. L.-M. Wong, D.-L. Ma, G. S.-M. Tong, K.-M. Ng, and C.-M. Che, "Cyclometalated Platinum(II) Complexes as Highly Sensitive Luminescent Switch-On Probes for Practical Application in Protein Staining and Cell Imaging," *Chemistry – A European Journal* 15 (2009): 3652–3656.

32. C.-K. Koo, K.-L. Wong, C. W.-Y. Man, et al., "A Bioaccumulative Cyclometalated Platinum(II) Complex with Two-Photon-Induced Emission for Live Cell Imaging," *Inorganic Chemistry* 48 (2009): 872–878.

33. C.-K. Koo, K.-L. Wong, C. W.-Y. Man, et al., "Two-Photon Plasma Membrane Imaging in Live Cells by an Amphiphilic, Water-Soluble Cyctometalated Platinum(II) Complex," *Inorganic Chemistry* 48 (2009): 7501.

34. C.-K. Koo, L. K.-Y. So, K.-L. Wong, et al., "A Triphenylphosphonium-Functionalised Cyclometalated Platinum(II) Complex as a Nucleolus-Specific Two-Photon Molecular Dye," *Chemistry – A European Journal* 16 (2010): 3942–3950.

35. A. J. Amoroso, R. J. Arthur, M. P. Coogan, et al., "3-Chloromethylpyridyl Bipyridine Fac-Tricarbonyl Rhenium: A Thiol-Reactive Luminophore for Fluorescence Microscopy Accumulates in Mitochondria," *New Journal of Chemistry* 32 (2008): 1097–1102.

36. A. J. Amoroso, M. P. Coogan, J. E. Dunne, et al., "Rhenium Fac Tricarbonyl Bisimine Complexes: Biologically Useful Fluorochromes for Cell Imaging Applications," *Chemical Communications* 43 (2007): 3066–3068.

37. M.-W. Louie, H.-W. Liu, M. H.-C. Lam, T.-C. Lau, and K. K.-W. Lo, "Novel Luminescent Tricarbonylrhenium(I) Polypyridine Tyramine-Derived Dipicolylamine Complexes as Sensors for Zinc(II) and Cadmium(II) Ions," *Organometallics* 28 (2009): 4297–4307.

38. M. D. Bartholomä, A. R. Vortherms, S. Hillier, et al., "Synthesis, Cytotoxicity and Cellular Uptake Studies of N_3 Functionalized $Re(CO)_3$ Thymidine Complexes," *Dalton Transactions (Cambridge, England: 2003)* 40 (2011): 6216–6225.

39. R. C. Evans, P. Douglas, and C. J. Winscom, "Coordination Complexes Exhibiting Room-Temperature Phosphorescence: Evaluation of Their Suitability as Triplet Emitters in Organic Light Emitting Diodes," *Coordination Chemistry Reviews* 250 (2006): 2093–2126.

40. P. J. Barnard, L. E. Wedlock, M. V. Baker, et al., "Luminescence Studies of the Intracellular Distribution of a Dinuclear Gold(I) N-Heterocyclic Carbene Complex," *Angewandte Chemie International Edition* 45 (2006): 5966–5970.

41. E. Vergara, E. Cerrada, A. Casini, O. Zava, M. Laguna, and P. J. Dyson, "Antiproliferative Activity of Gold(I) Alkyne Complexes Containing Water-Soluble Phosphane Ligands," *Organometallics* 29 (2010): 2596–2603.

42. P. J. Barnard, M. V. Baker, S. J. Berners-Price, and D. A. Day, "Mitochondrial Permeability Transition Induced by Dinuclear Gold(I)–carbene Complexes: Potential New Antimitochondrial Antitumour Agents," *Journal of Inorganic Biochemistry* 98 (2004): 1642–1647.

43. J. P. Rourke, A. S. Batsanov, J. A. K. Howard, and T. B. Marder, "Regiospecific High Yield Reductive Coupling of Diynes to Give a Luminescent Rhodium Complex," *Chemical Communications* 37 (2001): 2626–2627.

44. A. Steffen, M. G. Tay, A. S. Batsanov, et al., "2,5-Bis(*p* -R-arylethynyl) rhodacyclopentadienes Show Intense Fluorescence: Denying the Presence of a Heavy Atom," *Angewandte Chemie International Edition* 49 (2010): 2349–2353.

45. A. Steffen, K. Costuas, A. Boucekkine, et al., "Fluorescence in Rhoda- and Iridacyclopentadienes Neglecting the Spin–Orbit Coupling of the Heavy Atom: The Ligand Dominates," *Inorganic Chemistry* 53 (2014): 7055–7069.

46. A. Steffen, R. M. Ward, M. G. Tay, et al., "Regiospecific Formation and Unusual Optical Properties of 2,5-Bis(arylethynyl)rhodacyclopenta-dienes: A New Class of Luminescent Organometallics," *Chemistry – A European Journal* 20 (2014): 3652–3666.

47. C. Sieck, M. G. Tay, M.-H. Thibault, et al., "Reductive Coupling of Diynes at Rhodium Gives Fluorescent Rhodacyclopentadienes or Phosphorescent Rhodium 2,2′-Biphenyl Complexes," *Chemistry – A European Journal* 22 (2016): 10523–10532.

48. C. Sieck, D. Sieh, M. Sapotta, et al., "Convenient Synthetic Access to Fluorescent Rhodacyclopentadienes via Ligand Exchange Reactions," *Journal of Organometallic Chemistry* 847 (2017): 184–192.

49. Y.-M. Tian, X.-N. Guo, M. W. Kuntze-Fechner, et al., "Selective Photocatalytic C–F Borylation of Polyfluoroarenes by Rh/Ni Dual Catalysis Providing Valuable Fluorinated Arylboronate Esters," *Journal of the American Chemical Society* 140 (2018): 17612–17623.

50. P. S. Maharjan and H. K. Bhattarai, "Singlet Oxygen, Photodynamic Therapy, and Mechanisms of Cancer Cell Death," *Journal of Oncology* 2022 (2022): 7211485.

51. N. Singh, R. S. Gupta, and S. Bose, "A Comprehensive Review on Singlet Oxygen Generation in Nanomaterials and Conjugated Polymers for Photodynamic Therapy in the Treatment of Cancer," *Nanoscale* 16 (2024): 3243–3268.

52. J. E. Monat and J. K. McCusker, "Femtosecond Excited-State Dynamics of an Iron(II) Polypyridyl Solar Cell Sensitizer Model," *Journal of the American Chemical Society* 122 (2000): 4092–4097.

53. A. Cannizzo, F. van Mourik, W. Gawelda, G. Zgrablic, C. Bressler, and M. Chergui, "Broadband Femtosecond Fluorescence Spectroscopy of $[Ru(bpy)_3]^{2+}$," *Angewandte Chemie International Edition* 45 (2006): 3174–3176.

23670932, 2026, 8, Downloaded from https://chemistry-europe.onlinelibrary.wiley.com/doi/10.1002/cptc.70228 by Cochrane Croatia, Wiley Online Library on [24/11/2026]. See the Terms and Conditions (https://onlinelibrary.wiley.com/terms-and-conditions) on Wiley Online Library for rules of use; OA articles are governed by the applicable Creative Commons License

54. W. Gawelda, A. Cannizzo, V.-T. Pham, F. van Mourik, C. Bressler, and M. Chergui, "Ultrafast Nonadiabatic Dynamics of $[Fe^{II}(bpy)_3]^{2+}$ in Solution," *Journal of the American Chemical Society* 129 (2007): 8199–8206.

55. A. Cannizzo, A. M. Blanco-Rodríguez, A. El Nahhas, et al., "Femtosecond Fluorescence and Intersystem Crossing in Rhenium(I) Carbonyl–Bipyridine Complexes," *Journal of the American Chemical Society* 130 (2008): 8967–8974.

56. H. Yersin, *Transition Metal and Rare Earth Compounds III* (Springer Science & Business Media, 2004), 1–26.

57. Z. Guo, Y. Wang, J. Heitmüller, et al., "Ultrafast Photophysics of *para* -Substituted 2,5-bis(arylethynyl) Rhodacyclopentadienes: Thermally Activated Intersystem Crossing," *Chemical Science* 15 (2024): 14746–14756.

58. A. J. Morris, G. J. Meyer, and E. Fujita, "Molecular Approaches to the Photocatalytic Reduction of Carbon Dioxide for Solar Fuels," *Accounts of Chemical Research* 42 (2009): 1983–1994.

59. M. Montalti, A. Credi, L. Prodi, and M. T. Gandolfi, *Handbook of Photochemistry*, 3rd ed. (CRC Press, 2006).

60. H. Yersin, A. F. Rausch, R. Czerwieniec, T. Hofbeck, and T. Fischer, "The Triplet State of Organo-Transition Metal Compounds. Triplet Harvesting and Singlet Harvesting for Efficient OLEDs," *Coordination Chemistry Reviews* 255 (2011): 2622–2652.

61. P.-T. Chou, Y. Chi, M.-W. Chung, and C.-C. Lin, "Harvesting Luminescence via Harnessing the Photophysical Properties of Transition Metal Complexes," *Coordination Chemistry Reviews* 255 (2011): 2653–2665.

62. A. F. Rausch, H. H. H. Homeier, and H. Yersin, "Organometallic Pt(II) and Ir(III) Triplet Emitters for OLED Applications and the Role of Spin–Orbit Coupling: A Study Based on High-Resolution Optical Spectroscopy," *Topics in Organometallic Chemistry* 29 (2010): 193–235.

63. H. Yersin, "Topics in Current Chemistry," *Topics in Current Chemistry* 241 (2004): 1–26.

64. G. S. He, L.-S. Tan, Q. Zheng, and P. N. Prasad, "Multiphoton Absorbing Materials: Molecular Designs, Characterizations, and Applications," *Chemical Reviews* 108 (2008): 1245–1330.

65. F. Terenziani, C. Katan, E. Badaeva, S. Tretiak, and M. Blanchard-Desce, "Enhanced Two-Photon Absorption of Organic Chromophores: Theoretical and Experimental Assessments," *Advanced Materials* 20 (2008): 4641–4678.

66. M. Pawlicki, H. A. Collins, R. G. Denning, and H. L. Anderson, "Two-Photon Absorption and the Design of Two-Photon Dyes," *Angewandte Chemie International Edition* 48 (2009): 3244–3266.

67. H. M. Kim and B. R. Cho, "Two-Photon Materials With Large Two-Photon Cross Sections. Structure–Property Relationship," *Chemical Communications* 45 (2009): 153–164.

68. M. Rumi, S. Barlow, J. Wang, J. W. Perry, and S. R. Marder, *Photoresponsive Polymers I*, ed. S. R. Marder and K.-S. Lee (Springer, 2008), 1–95,

69. W. Denk, J. H. Strickler, and W. W. Webb, "Two-Photon Laser Scanning Fluorescence Microscopy," *Science (New York, N.Y.)* 248 (1990): 73–76.

70. H. M. Kim and B. R. Cho, "Small-Molecule Two-Photon Probes for Bioimaging Applications," *Chemical Reviews* 115 (2015): 5014–5055.

71. Q. Zhang, X. Tian, H. Zhou, J. Wu, and Y. Tian, "Lighting the Way to See Inside Two-Photon Absorption Materials: Structure–Property Relationship and Biological Imaging," *Materials* 10 (2017): 223.

72. P. Ning, W. Wang, M. Chen, Y. Feng, and X. Meng, "Recent Advances in Mitochondria- and Lysosomes-Targeted Small-Molecule Two-Photon Fluorescent Probes," *Chinese Chemical Letters* 28 (2017): 1943–1951.

73. W. R. Zipfel, R. M. Willams, and W. W. Webb, "Nonlinear Magic: Multiphoton Microscopy in the Biosciences," *Nature Biotechnology* 21 (2003): 1369–1377.

74. S. Yao and K. D. Belfield, "Two-Photon Fluorescent Probes for Bioimaging," *European Journal of Organic Chemistry* 2012 (2012): 3199–3217.

75. D. Kim, H. G. Ryu, and K. H. Ahn, "Recent Development of Two-Photon Fluorescent Probes for Bioimaging," *Organic & Biomolecular Chemistry* 12 (2014): 4550–4566.

76. S. Griesbeck, E. Michail, C. Wang, et al., "Tuning the π-Bridge of Quadrupolar Triarylborane Chromophores for One- and Two-Photon Excited Fluorescence Imaging of Lysosomes in Live Cells," *Chemical Science* 10 (2019): 5405–5422.

77. S. Griesbeck, E. Michail, F. Rauch, et al., "The Effect of Branching on the One- and Two-Photon Absorption, Cell Viability, and Localization of Cationic Triarylborane Chromophores with Dipolar versus Octupolar Charge Distributions for Cellular Imaging," *Chemistry – A European Journal* 25 (2019): 13164–13175.

78. S. Griesbeck, Z. Zhang, M. Gutmann, et al., "Water-Soluble Triarylborane Chromophores for One- and Two-Photon Excited Fluorescence Imaging of Mitochondria in Cells," *Chemistry – A European Journal* 22 (2016): 14701–14706.

79. A. Picot, A. D'Aléo, P. L. Baldeck, et al., "Long-Lived Two-Photon Excited Luminescence of Water-Soluble Europium Complex: Applications in Biological Imaging Using Two-Photon Scanning Microscopy," *Journal of the American Chemical Society* 130 (2008): 1532–1533.

80. J. L. Humphrey and D. Kuciauskas, "Charge Transfer Enhances Two-Photon Absorption in Transition Metal Porphyrins," *Journal of the American Chemical Society* 128 (2006): 3902–3903.

81. S. Das, A. Nag, D. Goswami, and P. K. Bharadwaj, "Zinc(II)- and Copper(I)-Mediated Large Two-Photon Absorption Cross Sections in a Bis-Cinnamaldiminato Schiff Base," *Journal of the American Chemical Society* 128 (2006): 402–403.

82. X.-B. Zhang, J.-K. Feng, and A.-M. Ren, "Theoretical Study of One- and Two-Photon Absorption Properties of Octupolar D_{2d} and D_3 Bipyridyl Metal Complexes," *Journal of Physical Chemistry A* 111 (2007): 1328–1338.

83. S. K. Hurst, M. G. Humphrey, T. Isoshima, et al., "Organometallic Complexes for Nonlinear Optics. 28. 1-Dimensional Evolution of Quadratic and Cubic Optical Nonlinearities in Stilbenylethynyl-ruthenium Complexes," *Organometallics* 21 (2002): 2024–2026.

84. E. Glimsdal, M. Carlsson, B. Eliasson, B. Minaev, and M. Lindgren, "Excited States and Two-Photon Absorption of Some Novel Thiophenyl Pt(II)–Ethynyl Derivatives," *Journal of Physical Chemistry A* 111 (2007): 244–250.

85. N. Jiang, J. Fan, F. Xu, et al., "Ratiometric Fluorescence Imaging of Cellular Polarity: Decrease in Mitochondrial Polarity in Cancer Cells," *Angewandte Chemie International Edition* 54 (2015): 2510–2514.

86. M. Li, J. Fan, H. Li, J. Du, S. Long, and X. Peng, "A Ratiometric Fluorescence Probe for Lysosomal Polarity," *Biomaterials* 164 (2018): 98–105.

87. S. Pinsuwan, A. Li, and S. H. Yalkowsky, "Correlation of Octanol/Water Solubility Ratios and Partition Coefficients," *Journal of Chemical & Engineering Data* 40 (1995): 623–626.

88. OECD, *Test No. 123: Partition Coefficient (1-Octanol/Water): Slow-Stirring Method, OECD Guidelines for the Testing of Chemicals, Section 1* (OECD Publishing, 2022).

89. M. Demeunynck, C. Bailly, and W. D. Wilson, ed., *Small Molecule DNA and RNA Binders: From Synthesis to Nucleic Acid Complexes* (Wiley-VCH Verlag GmbH & Co. KGaA, 2004).

90. J. D. McGhee and P. H. V. Hippel, "Theoretical Aspects of DNA-Protein Interactions: Co-Operative and Non-Co-Operative Binding of Large Ligands to a One-Dimensional Homogeneous Lattice," *Journal of Molecular Biology* 86 (1974): 469–489.

23670932, 2026, 8, Downloaded from https://chemistry-europe.onlinelibrary.wiley.com/doi/10.1002/cptc.70228 by Cochrane Croatia, Wiley Online Library on [24/11/2026]. See the Terms and Conditions (https://onlinelibrary.wiley.com/terms-and-conditions) on Wiley Online Library for rules of use; OA articles are governed by the applicable Creative Commons License

91. O. Dömötör, F. Binacchi, N. Ribeiro, et al., "How Reliable Is the Evaluation of DNA Binding Constants? Insights and Best Practices Based on an Inter-Laboratory Fluorescence Titration Study," *Spectrochimica Acta Part A: Molecular and Biomolecular Spectroscopy* 327 (2025): 125354.

92. G. Horvat and I. Piantanida, "Comprehensive Tutorial: Characterization of Small Molecule–DNA Noncovalent Binding Interactions," *Croatica Chemica Acta* 99, no. 1 (2026): P1–P29, https://doi.org/10.5562/cca4215.

93. J. L. Mergny and L. Lacroix, "Analysis of Thermal Melting Curves," *Oligonucleotides* 13 (2003): 515–537.

94. W. D. Wilson, L. Ratmeyer, M. Zhao, L. Strekowski, and D. Boykin, "The Search for Structure-Specific Nucleic Acid-Interactive Drugs: Effects of Compound Structure on RNA versus DNA Interaction Strength," *Biochemistry* 32 (1993): 4098–4104.

95. A. Rodger and B. Norden, *Circular Dichroism and Linear Dichroism* (Oxford University Press, 1997).

96. T. Šmidlehner, I. Piantanida, and G. Pescitelli, "Polarization Spectroscopy Methods in the Determination of Interactions of Small Molecules with Nucleic Acids – Tutorial," *Beilstein Journal of Organic Chemistry* 14 (2018): 84–105.

97. M. Eriksson and B. Norden, "Methods in Enzymology," *Methods in Enzymology* 340 (2001): 68–98.

98. N. C. Garbett, P. A. Ragazzon, and J. B. Chaires, "Circular Dichroism to Determine Binding Mode and Affinity of Ligand–DNA Interactions," *Nature Protocols* 2 (2007): 3166–3172.

99. N. Holmgaard List, J. Knoops, J. Rubio-Magnieto, et al., "Origin of DNA-Induced Circular Dichroism in a Minor-Groove Binder," *Journal of the American Chemical Society* 139 (2017): 14947.

100. L. A. Reis and M. S. Rocha, "DNA Interaction with DAPI Fluorescent Dye: Force Spectroscopy Decouples Two Different Binding Modes," *Biopolymers* 107 (2017): e23015.

101. S. Y. Breusegem, R. M. Clegg, and F. G. Loontiens, "Base-Sequence Specificity of Hoechst 33258 and DAPI Binding to Five (a/T)4 DNA Sites with Kinetic Evidence for More than One High-Affinity Hoechst 33258-AATT Complex," *Journal of Molecular Biology* 315 (2002): 1049–1061.

102. S.-K. Leung, K. Y. Kwok, K. Y. Zhang, and K. K.-W. Lo, "Design of Luminescent Biotinylation Reagents Derived from Cyclometalated Iridium(III) and Rhodium(III) Bis(pyridylbenzaldehyde) Complexes," *Inorganic Chemistry* 49 (2010): 4984–4995.

Supporting Information

Additional supporting information can be found online in the Supporting Information section. All synthetic procedures, analytical data, photophysical studies, crystallographic, cell imaging, biomolecule sensing, and computational data are available in the supplementary material of this article. The authors have cited additional references within the Supporting Information [87, 88, 91, 92, 103–117].

23670932, 2026, 8, Downloaded from https://chemistry-europe.onlinelibrary.wiley.com/doi/10.1002/cptc.70228 by Cochrane Croatia, Wiley Online Library on [24/11/2026]. See the Terms and Conditions (https://onlinelibrary.wiley.com/terms-and-conditions) on Wiley Online Library for rules of use; OA articles are governed by the applicable Creative Commons License